

The DREAMS Experiment Onboard the Schiaparelli Module of the ExoMars 2016 Mission: Design, Performances and Expected Results

F. Esposito¹  · S. Debei² · C. Bettanini² · C. Molfese¹ · I. Arruego Rodríguez³ · G. Colombatti² · A.-M. Harri⁴ · F. Montmessin⁵ · C. Wilson⁶ · A. Aboudan² · P. Schipani¹ · L. Marty¹ · F.J. Álvarez³ · V. Apestigue³ · G. Bellucci⁷ · J.-J. Berthelier⁵ · J.R. Brucato⁸ · S.B. Calcutt⁶ · S. Chiodini² · F. Cortecchia⁹ · F. Cozzolino¹ · F. Cucciarrè² · N. Deniskina¹ · G. Déprez⁵ · G. Di Achille¹⁰ · F. Ferri² · F. Forget¹¹ · G. Franzese^{1,12} · E. Friso² · M. Genzer⁴ · R. Hassen-Kodja⁵ · H. Haukka⁴ · M. Hieta⁴ · J.J. Jiménez³ · J.-L. Josset¹³ · H. Kahanpää⁴ · O. Karatekin¹⁴ · G. Landis¹⁵ · L. Lapauw⁵ · R. Lorenz¹⁶ · J. Martinez-Oter³ · V. Mennella¹ · D. Möhlmann¹⁷ · D. Moirin⁵ · R. Molinaro¹ · T. Nikkanen⁴ · E. Palomba⁷ · M.R. Patel¹⁸ · J.-P. Pommereau⁵ · C.I. Popa¹ · S. Rafkin¹⁹ · P. Rannou²⁰ · N.O. Renno²¹ · J. Rivas³ · W. Schmidt⁴ · E. Segato² · S. Silvestro¹ · A. Spiga¹¹ · D. Toledo²² · R. Trautner²³ · F. Valero²⁴ · L. Vázquez²⁴ · F. Vivat⁵ · O. Witasse²³ · M. Yela³ · R. Mugnuolo²⁵ · E. Marchetti²⁵ · S. Pirrotta²⁵

Received: 5 December 2016 / Accepted: 5 August 2018
© Springer Nature B.V. 2018

ExoMars-16
Edited by Håkan Svedhem and Christopher T. Russell

✉ F. Esposito
francesca.esposito@inaf.it

¹ Osservatorio Astronomico di Capodimonte, INAF, Salita Moiarriello 16, 80131 Naples, Italy

² CISAS, Università degli Studi di Padova, Padova, Italy

³ INTA, Madrid, Spain

⁴ Finnish Meteorological Institute (FMI), Helsinki, Finland

⁵ LATMOS, CNRS/UVSQ/IPSL, Paris, France

⁶ Oxford University, Oxford, UK

⁷ Istituto di Astrofisica e Planetologia Spaziali (IAPS), INAF, Rome, Italy

⁸ Osservatorio Astrofisico di Arcetri, INAF, Firenze, Italy

⁹ Osservatorio di Astrofisica e Scienza dello Spazio di Bologna (OAS), INAF, Bologna, Italy

¹⁰ Osservatorio Astronomico di Teramo, INAF, Teramo, Italy

¹¹ Laboratoire de Météorologie Dynamique, UMR CNRS 8539, Institut Pierre-Simon Laplace, Sorbonne Universités, UPMC Univ Paris 06, Centre National de la Recherche Scientifique, Paris, France

¹² Department of physics, University of Naples “Federico II”, Naples, Italy

Abstract The first of the two missions foreseen in the ExoMars program was successfully launched on 14th March 2016. It included the Trace Gas Orbiter and the Schiaparelli Entry descent and landing Demonstrator Module. Schiaparelli hosted the DREAMS instrument suite that was the only scientific payload designed to operate after the touchdown. DREAMS is a meteorological station with the capability of measuring the electric properties of the Martian atmosphere. It was a completely autonomous instrument, relying on its internal battery for the power supply. Even with low resources (mass, energy), DREAMS would be able to perform novel measurements on Mars (atmospheric electric field) and further our understanding of the Martian environment, including the dust cycle. DREAMS sensors were designed to operate in a very dusty environment, because the experiment was designed to operate on Mars during the dust storm season (October 2016 in Meridiani Planum). Unfortunately, the Schiaparelli module failed part of the descent and the landing and crashed onto the surface of Mars. Nevertheless, several seconds before the crash, the module central computer switched the DREAMS instrument on, and sent back housekeeping data indicating that the DREAMS sensors were performing nominally. This article describes the instrument in terms of scientific goals, design, working principle and performances, as well as the results of calibration and field tests. The spare model is mature and available to fly in a future mission.

Keywords ExoMars · Schiaparelli · DREAMS · Mars · Atmospheric electric field · Meteorological station · Dust storm season

1 Introduction

The European Space Agency (ESA) has been executing the ExoMars program in cooperation with the Russian federal Space Agency (Roscosmos). It foresees two elements: the first one, launched on 14th March 2016 from Baikonur in Kazakhstan, includes the Trace Gas Orbiter (TGO), currently in orbit around Mars, and the Schiaparelli lander demonstrator that unfortunately did not land safely. The second mission will be launched in the 2020; it includes a Russian Surface Platform and a European rover. The whole program will allow Europe to mature the technologies necessary for the entry, descent and landing of a payload

¹³ Space Exploration Institute, Neuchâtel, Switzerland

¹⁴ Royal Observatory of Belgium, Uccle, Belgium

¹⁵ GRC, NASA, Cleveland, USA

¹⁶ JHU Applied Physics Lab (JHU-APL), Laurel, USA

¹⁷ DLR PF Leitungsbereich, Berlin, Germany

¹⁸ Open University, Milton Keynes, UK

¹⁹ Southwest Research Institute, San Antonio, USA

²⁰ GSMA, Paris, France

²¹ University of Michigan, Ann Arbor, USA

²² Reims Champagne-Ardenne University, Reims, France

²³ ESA-ESTEC, Noordwijk, The Netherlands

²⁴ Universidad Complutense de Madrid (UCM), Madrid, Spain

²⁵ Italian Space Agency, Rome, Italy

on the surface of Mars, to move on the Martian surface with a rover, to penetrate into the subsurface and acquire samples and to distribute the collected samples to on-board instruments for analysis. From the scientific point of view, the ExoMars program will search for signs of extant or extinct life forms, will monitor trace gases in the atmosphere of Mars and their sources, will investigate how the water and geochemical environment varies, will monitor long-term climate and will perform atmospheric investigations (Vago et al. 2015).

The 2016 mission arrived at Mars on 19th October 2016. The TGO successfully entered into Martian orbit and started the acquisition of scientific data around the end of November. Its main scientific objectives are to monitor methane and other trace gases and their sources on the surface of Mars. Since living organisms produce most of the methane present in the terrestrial atmosphere, the science community has interest in the monitoring of this gas on Mars (Formisano et al. 2004; Mumma et al. 2009; Webster et al. 2015).

While TGO successfully entered into Martian orbit on 19th October, unfortunately the Schiaparelli module failed to land safely. This module carried the DREAMS (*Dust characterization, Risk assessment and Environment Analyzer on the Martian Surface*) instrument, that was supposed to start to operate after the touchdown in Meridiani Planum, an active area from the aeolian point of view (Chojnacki et al. 2017; Silvestro et al. 2011, 2015; Bridges et al. 2013). A few seconds before crashing onto the surface of Mars, Schiaparelli started the sequence of operations foreseen after landing and switched on DREAMS that proved to be healthy and ready to start measurements.

DREAMS is a meteorological station, conceived with a modular architecture, with the capability of performing measurements of the electric field close to the surface of Mars. It is an autonomous system that includes its own battery to supply power. It includes the following subsystems (see Sect. 2): MarsTEM (thermometer), DREAMS-P (pressure sensor), DREAMS-H (humidity sensor), MetWind (2-D wind sensor), MicroARES (electric field sensor), SIS (Solar Irradiance Sensor), a CEU (Central Electronic Unit) and a battery. It was designed to operate in very extreme conditions such as during the dust storm season, when it was supposed to land.

DREAMS is mature and available for a future mission in order to perform:

- Meteorological measurements
 - The measurements of pressure, temperature, wind speed and direction, humidity and dust opacity enable to characterize the basic state meteorology and its daily variation at the landing site.
 - Such information can directly be compared to climate models.
 - DREAMS is equipped to characterize the Martian boundary layer, also in dusty conditions.
- Hazard monitoring
 - DREAMS can provide a comprehensive dataset to help engineers to quantify hazards for equipment and human crew: velocity of windblown dust, electrostatic charging, existence of discharges, electromagnetic noise potentially affecting communications, intensity of UV radiation.
- Monitor of atmospheric electric phenomena
 - A global atmospheric electrical circuit is likely to exist on Mars, between the surface and the ionosphere, with similarities and differences with the Earth's circuit (Aplin 2006). Atmospheric ionization should be similar to that of the Earth's stratosphere but impact charging through collisions between dust particles moved by the wind and the surface, or between dust particles themselves, is expected to be the dominant charging mechanism. Intense electric fields, possibly capable of producing electrical breakdown, are expected at the time of dust storms and in the vicinity of dust devils.

- Atmospheric electricity is also involved in several processes that have a noticeable impact on the surface and atmosphere. At times of dust storms, electrostatic forces on fine electrically charged dust grains may become larger than aerodynamic forces due to the wind. They are expected to play a significant role in the dynamics (including lifting) of suspended dust particles and their interaction with the surface, thus on the processes that contribute to the erosion and long-term evolution of the surface (Esposito et al. 2016; Harrison et al. 2016; Murphy et al. 2016).
- By energizing the free electrons, the atmospheric electric field controls their interaction with both the surface and the atmospheric gases. They have thus a definite role in the chain of physical and chemical processes that govern the chemical state of surface materials and the production of oxidized constituents in the atmosphere with implications on the sustainability of proper conditions for life (Atreya et al. 2006).

A Flight Spare model of DREAMS is mature and available for a future mission.

Some of the DREAMS sensors have been tested in the Sahara desert during the dust storm season to prove their ability to work in a dusty environment and to probe dust events. The field campaign allowed also the advancement of our knowledge of Aeolian processes and their relation with the electric properties of the atmosphere.

The following sections describe the DREAMS instrument design, sensors performance, and calibration procedures. Results of the field tests are described in Sect. 4.

2 The DREAMS Experiment

The DREAMS experiment is the result of a cooperation of six European Countries (Italy, France, Spain, Netherlands, Finland, United Kingdom) led by Italy. The team organization is described in Fig. 1.

DREAMS (Fig. 2) is a completely autonomous sensor suite containing the following sub-systems: (a) the power unit (a space qualified rechargeable battery assembly developed by ABSL), (b) the Central Electronic Unit (CEU), comprising all electronic boards for sensor data acquisition and communication with Schiaparelli module, (c) the MetMast assembly (about 20.4 cm tall) which hosts most of the external sensors and (d) the MicroARES electrode (27 cm tall).

A dedicated harness guarantees the connection of DREAMS hardware located in the internal bay with the external sensing units and the Schiaparelli control unit through a connector bracket which interfaces the internal compartment with the external environment.

The following subsections describe each DREAMS element.

2.1 DREAMS-H

DREAMS-H (Fig. 3) is a miniature relative humidity measurement device based on technology developed by the Finnish company Vaisala, Inc. DREAMS-H is functionally and electrically almost an exact copy of REMS-H instrument onboard MSL/Curiosity (Harri et al. 2014b). The mass of DREAMS-H is approx. 15 g and the power consumption is 15 mW.

As REMS-H, DREAMS-H measures relative humidity with 3 Humicap[®] polymeric capacitive sensor heads, while accurate temperature measurements required for interpretation of relative humidity measurements are provided with capacitive Thermocap[®] sensor heads, both by Vaisala, Inc. The sensor heads are placed on a single PCB together with proximity electronics, and protected with metallic Faraday cage. The cage is perforated to allow

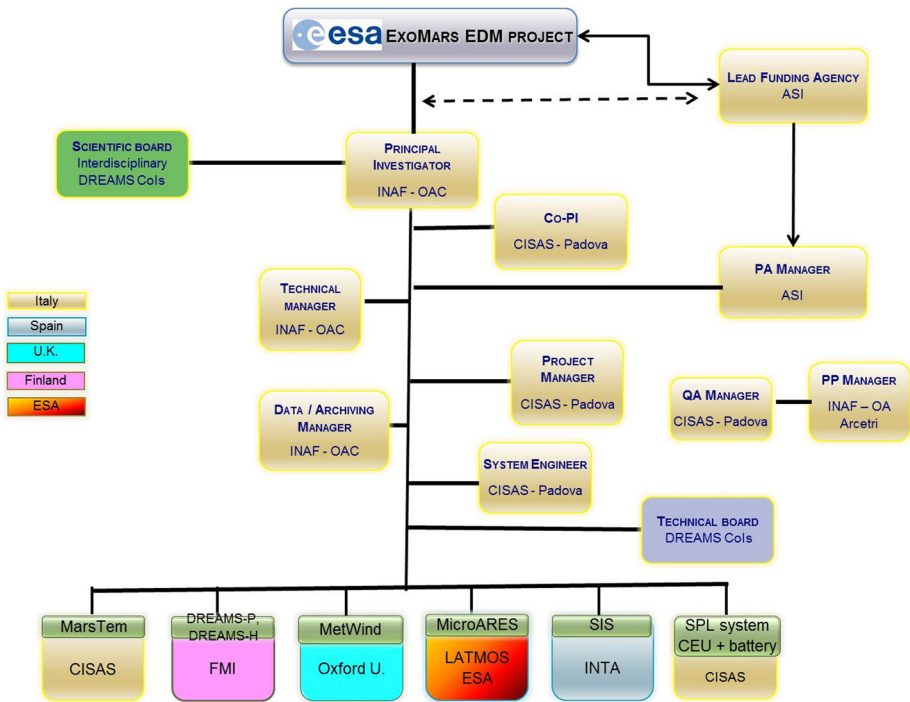


Fig. 1 DREAMS team organization

gas exchange between the sensor heads and the surrounding environment. To protect the sensor from excessive dust, part of the holes are covered with a PTFE filter material. The whole structure is mounted on DREAMS mast at about 17 cm height from the top of Schiaparelli Central Bay. DREAMS-H control and data retrieval is handled by the measurement controller located on the DREAMS-P PCB.

The Humicap[®] sensor heads contain an active polymer that changes its capacitance as function of relative humidity and temperature with 0 to 100% RH measurement range. In a given temperature, the response between 0 and 100%RH is very close to linear. The polymer reacts to the relative humidity even when the device is not powered, so the relative humidity can be read almost immediately after power-on.

Nominal capacitance of Humicap[®] is in order of 6 pF. The dynamic range of the Humicap[®] changes with temperature, being approx. 1 pF around 273 K and approx. 0.3 pF around 203 K. The Humicap[®] also becomes logarithmically slower with lower temperature, its time constant is about 0.1 s at 293 K, but for example at 233 K it is about 30 s and at 203 K about 700 s. Some additional time lag is added also by the protective PTFE filter. The time lag caused by the coldness and PTFE filter can be partially mathematically compensated on ground. The compensation algorithm is based on the relative humidity reading and its speed of change. The basis of this method is the fact that the speed of change through the filter depends on the atmospheric temperature and the difference of RH between the inside and the outside. Therefore, the difference in RH can be calculated by knowing the ambient temperature, and the speed of the change in raw RH values (Harri et al. 2014b).

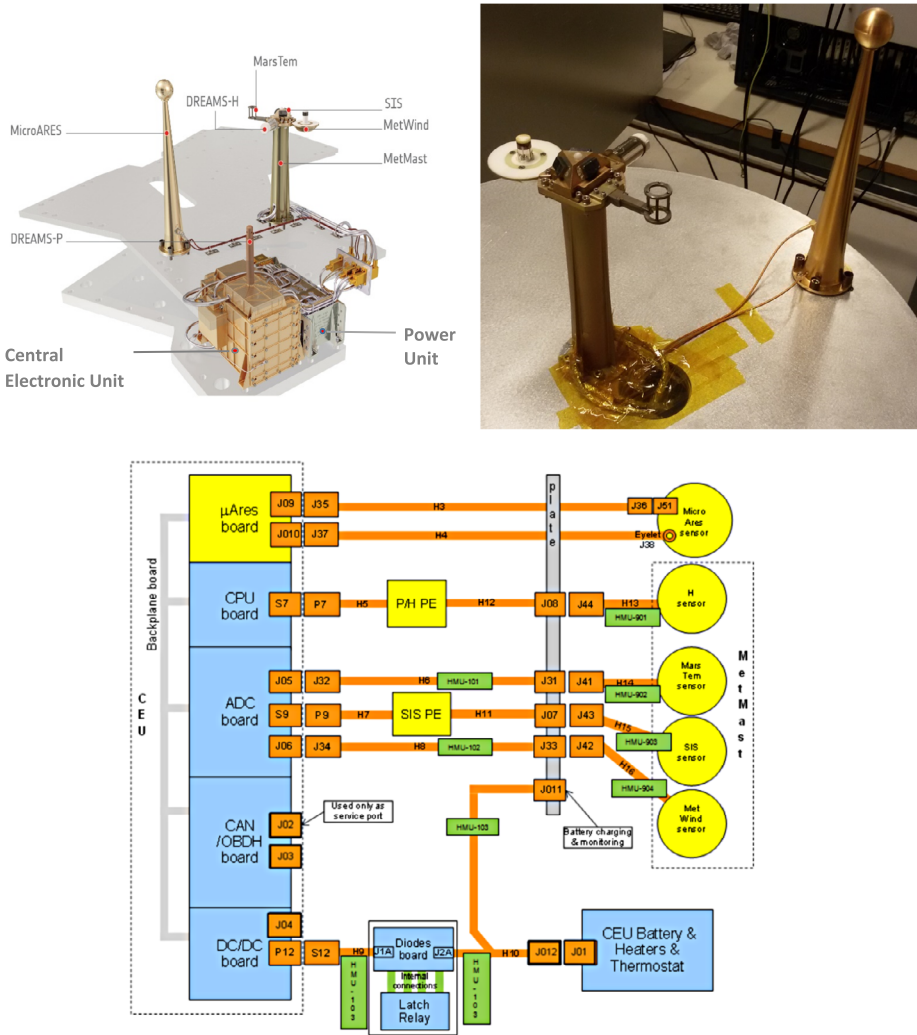


Fig. 2 Top left: graphic impression of the DREAMS instrument and its location in the Schiaparelli Central Bay. Credit: ESA. Top right: DREAMS spare model: MetMast (on the left) and MicroARES antenna (on the right). Bottom: DREAMS block diagram

2.2 DREAMS-P

DREAMS-P is a miniature pressure sensor designed for making accurate measurements in the Martian atmosphere surface pressure range. The device houses two pressure transducers and an integrated measurement controller, which controls the DREAMS-P pressure and DREAMS-H humidity measurements (Fig. 4).

The pressure device is based on capacitive Barocap® sensor heads manufactured by Vaisala, Inc. The whole DREAMS-P device is mounted inside the lander warm compartment, with the pressure transducer electronics being housed inside a Faraday shield, a rectangular enclosure made of copper covered Printed Circuit Boards, to protect the electronics

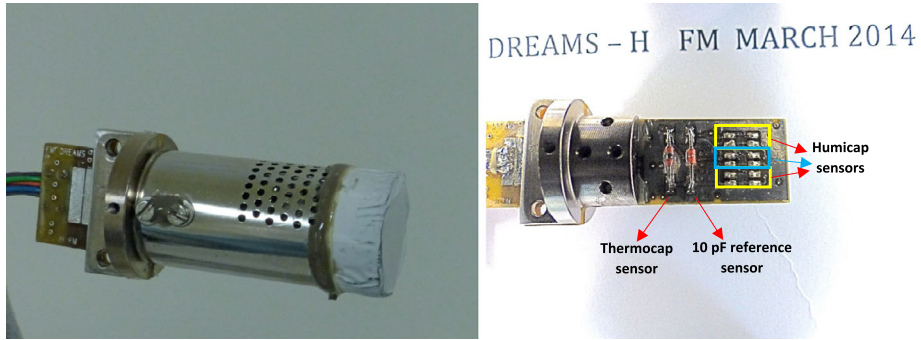


Fig. 3 DREAMS-H sensor. Credit: FMI/Markku Mäkelä

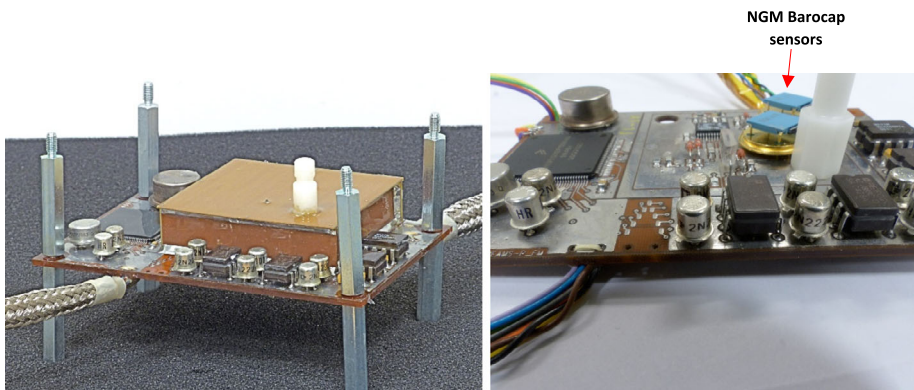


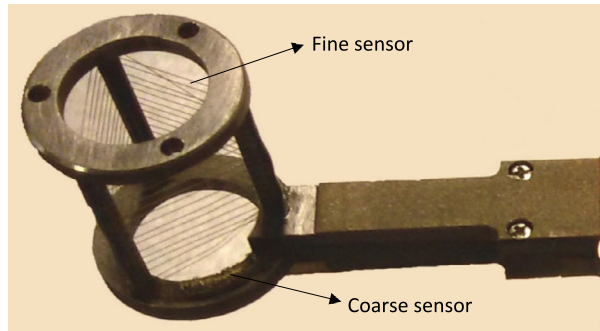
Fig. 4 DREAMS-P sensor with (left panel) and without (right panel) the cover. Credit: FMI/Markku Mäkelä. The components with blue parts in the right panel are NGM Barocaps. The RSP2Ms are on the other side of the board

from electromagnetic interference. Atmospheric ambient pressure is led inside the device through a pipe protruding above the lander deck. The top part of pipe outlet is designed to prevent excessive amounts of dust from entering the system.

The device consists of two pressure transducers with heritage from the REMS-P instrument flown onboard the Curiosity rover (Harri et al. 2014a). Each transducer has two Barocap[®] pressure sensor heads, two Thermocap[®] temperature sensor heads and four constant capacitors for reference. The DREAMS-P2 transducer is essentially identical to the electrical design in REMS-P using the Barocap[®] RSP2M sensor heads, while the DREAMS-P1 transducer utilizes the “new generation” NGM sensor heads by Vaisala, specifically modified for Martian pressure range. This sensor head replaces the now obsolete “LL” sensor head used in Phoenix pressure sensor and REMS. The NGM has no previous flight heritage, but it has been fully qualified for spaceflight during DREAMS testing and qualification campaign.

The pressure dependence of Barocap[®] capacitance is opposite in RSP2M and NGM. In RSP2M, higher ambient pressure pushes the capacitor plates inside the sensor head further away from each other, thus lowering the capacitance. In NGM, one of the capacitor plates is at the bottom of the vacuum cavity inside the sensor head, and so higher ambient pressure pushes the capacitor plates closer to each other, increasing the capacitance until the plates

Fig. 5 MarsTEM sensor with the fine and coarse subsystems indicated



touch in approx. 70 hPa and the sensor head is shorted. Thus NGM can only be measured in low pressures below this limit.

The RSP2M sensors offer fast warm up time and high resolution, which means that they are very suitable for short intermittent measurements. The new NGM sensors offer even better resolution and long term stability than the RSP2Ms, but require a longer warm up period in the beginning of each measurement sequence.

A low-power measurement controller is integrated on the DREAMS-P device circuit board. The controller is based on the Freescale MC9S12XEP100 automotive commercial-off-the-shelf microcontroller (MCU). The MCU was qualified for use as part of Mars lander missions by a custom qualification process led by the Finnish Meteorological Institute (Nikkanen et al. 2015). The measurement controller provides power and control signals for the integrated pressure transducers and the external humidity transducer. The DREAMS CEU issues telecommands to and receives measurement telemetry and instrument status from the DREAMS-P controller through a RS-422 data interface. During measurements, the active transducer acts as a multiplexed RC oscillator and generates a set of eight frequency signals. Pressure or humidity readings are obtained by data analysis after defining the frequencies on these transducer sensor and reference channels. A stable reference crystal clock frequency is utilized to measure the duration of a given amount of sensor or reference channel pulses to derive each measurement channel frequency.

2.3 MarsTEM

MarsTEM is a platinum Resistance Temperature Detector (RTD) for the measurement of the atmospheric temperature at the surface of Mars (Colombatti et al. 2014).

In order to measure the temperature, the convective flux is detected by a thin ($\phi = 0.0508$ mm) and long platinum wire ($L = 700$ mm) which lead to a resistance of 37.8 ohm @ 0 °C and a time constant of 0.3 seconds at a wind speed of 5 m/s and absolute pressure of 6 hPa.

The sensor wire is wounded on an insulating structure (Titanium alloy) to minimize the conductive heat flux from the sensor wire and structure. The structure hosts a secondary Platinum RTD, made from the same thin wire of the primary, which provides redundancy (e.g. in case the wounded sensor is damaged by dust). Simultaneous acquisition of both sensors allows for the dynamical correction of primary sensor in data post-processing (Fig. 5). In addition, from the retrieved titanium structure time constant, the secondary thermometer will support the correction of errors introduced by solar radiation contribution on the primary sensor. Chiodini et al. (2014) showed that the radiative contribution of the thermal

flux on the sensor is lower than 30% at noon conditions (the worst from this point of view) with a wind of 1 m/s and that this contribution decreases to 20% with a 5 m/s wind. The radiative flux contribution produces an increase of about 1.5 °C in the temperature of the sensing element. Anyway, most of this contribution is due to the radiative flux arriving on the sensor from the structure itself and not directly from the sun. Similar increase in temperature has also been observed in the test field performed in the Moroccan desert (Colombatti et al. 2015). Primary and secondary sensors are sensed with a 3-wires configuration circuit allowing conditioning and acquisition of voltage through the DREAMS electronics.

To minimize the self-heating and to achieve anyway high electrical sensitivity, the sensors are powered with a pulsed current profile. In such a way the rms current value is very low, which means negligible joule effect, while instantaneous current value is high to maximize the sensors electrical sensitivity. MarsTEM design and realization, including its conditioning circuitry, were validated through the Missus Experiment flown on BEXUS15 ESA/SSC/DLR stratospheric balloon, which hosted the sensor prototype and the conditioning circuitry.

The terrestrial absolute pressure at about 30 km of altitude is an analogue of Martian pressure at the surface. Missus allowed the validation of the mathematical model (even of sun irradiance effects) and the tuning of the electrical current profile in order to maximize sensitivity/self-heating ratio and the overall SNR. To infer MarsTEM performance from MISSUS experiment results, the comparison between Earth and Mars potential temperature was performed (Chiodini et al. 2014).

MarsTEM performances were obtained during calibration within the range -100 °C $+20$ °C.

2.4 MetWind

MetWind is a thermal anemometer that measures the components of wind speed and direction in the plane perpendicular to the sensor axis. The sensor head consists of three thin-film platinum heat transfer gauges, equally spaced around the circumference of a vertical cylinder (Fig. 6). Each film is resistively heated using a constant current raising its temperature above the ambient air. The film's electrical resistance is measured, allowing calculation of the temperature and thus the heat transfer coefficient at each hot film. The differences in heat transfer coefficients between the three films is used to calculate a two-dimensional wind vector perpendicular to the axis of the wind sensor. In its normal orientation the axis of the central cylinder is vertical, so that the sensor measures a horizontal wind vector. The sensor is calibrated for the range of 0.3–30 m/s although wind speeds above this range can be measured as well.

Thermal wind sensors have a long heritage on Mars. These include the Viking Lander wind sensors; the Mars Pathfinder wind sensor, Mars Polar Lander wind sensor, and the Mars Science Laboratory wind sensor. Principle advantages of thermal anemometry are the low mass and simplicity of thermal wind sensors. Balanced against this advantage is the fact that thermal wind sensors are difficult to calibrate, because they are sensitive not only to wind but also to other thermal loads, such as those caused by changes in air temperature and solar illumination.

MetWind reuses the Beagle 2 Wind Sensor design (Towner et al. 2004; Wilson et al. 2003), with the addition of a housekeeping sensor: a platinum resistance thermometer that has been placed in the center of the sensor. The data from this thermometer supports the calculation of the conductive heat losses, which would otherwise be one of the largest sources of uncertainty in interpreting the wind speed data.

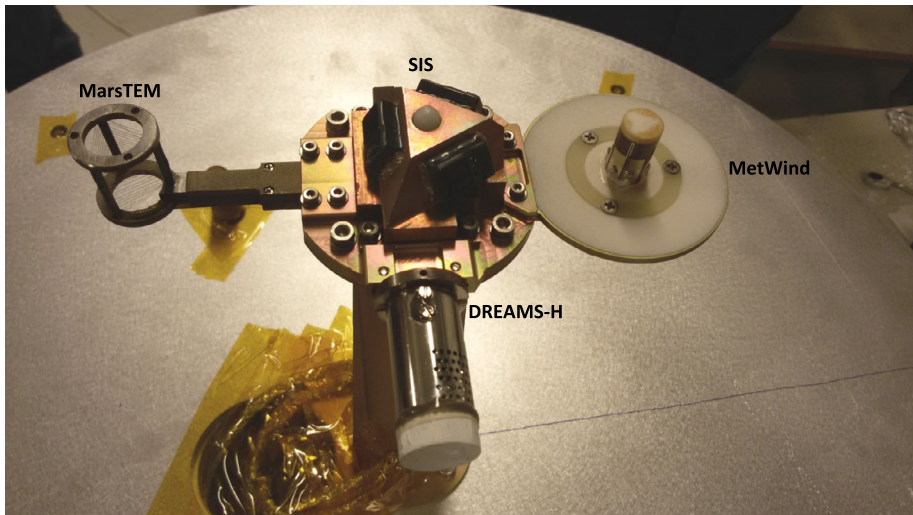


Fig. 6 MetMast top view

The MetWind thermal anemometry technology is similar to that used on Mars Pathfinder (Seiff et al. 1997). Wind speed data acquired by the Mars Pathfinder sensor has not been published because of large uncertainty in the overheat ($T_{wire} - T_{air}$), which in turn was caused by large fluctuations in the air temperature (up to ± 10 °C during the day). This air temperature fluctuation is large in comparison to the overheat of the sensor wire, which was only 1–10 °C for the Pathfinder sensor. The overheat of the Beagle 2 wind sensor's hot films would have been typically 50–70 °C, and for MetWind this was increased to 70–85 °C by adjusting resistances; this greater overheat reduces the measurement error in wind speed.

The MetWind electronics are designed to allow two sensing modes. The first is a low-current mode ('TEMP' mode), in which only 1 mW of heating power is dissipated in the films. In this mode the self-heating is only ~ 2 °C, and is relatively insensitive to wind speed. In this mode, therefore, the wind sensors can be used to provide a backup measurement of air temperature; it also provides a way of check whether the film resistances have changed with time, for example due to sand abrasion.

On power-up, the electronics are typically started in the low power (TEMP) mode. After 30 seconds, MetWind is switched to high power mode (WIND) mode, in which ~ 40 mW are dissipated in each film. The electronics then remain in WIND mode until they are next powered off and back on again.

The response time of the sensor to step changes in wind speed is ~ 2 –5 seconds, dependent on wind speed and direction. This is sufficient to allow characterization of large-eddy turbulence and detection of convective vortices.

MetWind is extremely light: the sensor head itself weighs only 0.7 grams. Once its mounting screws and 400 mm harness are taken into account the total mass is 11 grams, excluding connectors and electronics (which are included in the CEU). Total power consumption while sensing wind is around 250 mW, of which 120 mW are dissipated in the sensor head.

2.5 MicroARES

Micro-ARES is a single probe electric field instrument consisting of a spherical electrode installed on a stiff metallic support (Fig. 2) and a single electronics board housed in the common electronics box (DREAMS CEU) placed in the warm compartment.

The predecessor of MicroARES called ARES (proposed in a double probe version, see for instance Berthelier et al. 2000) has been validated on two balloon flights and was developed as part of the HUMBOLDT platform payload (and successfully passed the Preliminary Design Review) in a previous configuration of the ExoMars mission.

MicroARES measures the amplitude of the vertical component of the electric field in the atmosphere, with the lander potential as reference. A high impedance ($10^{14} \Omega$) preamplifier is mounted in a voltage follower configuration yielding a precise measurement of the surrounding atmospheric potential; the Mars near surface atmosphere is a medium whose typical resistivity is > 10 smaller than the MicroARES instrument impedance (Farrell et al. 2015).

In the Analog portion of the electronics board, the signal is separated in two components: (1) the large amplitude (mV to V) and low frequency (< 10 Hz) signal of the DC channel and (2) the small amplitude (10^{-3} mV) and high frequency (100 Hz to kHz) signal of the AC channel. The difference between the two resides in the capacitive coupling of the AC channel with the antenna, which effectively suppresses the main component of the signal received from the sphere. The high sensitivity of the AC channel can be used to detect the impacts of charged dust particles to let one infer their horizontal flux and charge distribution.

A high voltage mode is automatically activated by the Micro-ARES central computer (a Texas Instrument[®] Digital Signal Processor, hereafter referred as to DSP) when the modulus of the acquired potential exceeds 90 V for a certain amount of time (typically a fraction of second). This high voltage mode disrupts the equilibrium of potentials between the antenna and the atmosphere by bifurcating the input signal into a resistive bridge dividing the signal by a factor of > 50 and forcing it to cope with the voltage range admitted by the 16 bits ADC.

When operated in the *relaxation probe mode*, the instrument measures the atmospheric conductivity separately for positive and negative ions. Periodically, +1 V and -1 V pulses are sequentially injected by capacitors into the antenna, creating a small and temporary departure from equilibrium between the potential of the antenna and that of the atmosphere surrounding it. Positive and negative ions flowing around the electrode are then attracted by the antenna surface depending on the pulse polarity to fill in the gap of potentials with a characteristic e-folding relaxation time. This provides data for estimating the positive and negative conductivities.

MicroARES computing capabilities are ensured by a Digital Signal Processor (DSP) from Analog Devices[®] (model ADSP-2189). This DSP has a 13 ns instruction cycle time and can handle 75 MIPS. It is particularly notable for its large on-chip memory (1.5 Mbits) and its low power features (2.5 V). As the ADSP-2189 cannot be procured in a space-qualified version, it received the needed screening and qualification (Construction analysis, Highly Accelerated Stress Tests, Life test, Single Event Effects and Total Ionisation Dose testings) to verify that proper operations would be carried out once at Mars. The main DSP tasks are setups and commands of the analog part, real time signal processing (data decimation, filtering, selection and conditioning), and ensures communication with the CEU.

2.6 SIS

SIS (Solar Irradiance Sensor) is a radiometer designed to measure solar irradiance on the Martian surface. Its main goals are: (a) to provide an estimation of the atmospheric optical depth (OD) and its variations within a Sol; (b) to allow for the detection of clouds through the analysis of the shape of the ratio between the signals measured in two different spectral bands (UV and NIR) during twilight; and (c) to provide a direct measurement of the global irradiance on the surface.

It consists of two units, an optical head (OH) and a processing electronics (PE) box. OH (Fig. 7) contains the detecting elements and front-end electronics, whereas PE acquires and digitizes the signals provided by the OH, controls the sensor and communicates with the CEU. OH is located on top of the DREAMS MetMast (Fig. 2, Fig. 6). This placement severely constrained the OH mass to less than 26 g. OH contains 7 different silicon photodetectors distributed on 4 faces: one bare silicon detector with a spectral response of 200–1100 nm pointing to the instrument's zenith, and three pairs of "lateral" detectors covered with filters in the UV and NIR bands (UV: 315–400 nm; NIR: 700–1100 nm), pointing to an elevation of 30 degrees and azimuths of 60, 180 and 300 degrees within the OH reference frame. The detectors are commercial-of-the-shelf photodiodes that are covered with custom interference filters to provide the desired spectral response. OH contains an eighth detector inside its mechanical assembly, covered by a lid to inhibit light reception. The dark current of this detector is measured to estimate the displacement damage suffered during the trip to Mars (Jimenez et al. 2012). Each lateral detector is covered by an interference filter and a mechanical mask that provides the desired Field-of-View (FoV). This FoV is around ± 40 degrees when measured to a 10% of the maximum responsivity. The zenith detector is covered with a diffusing dome that provides a quasi-planar hemispherical FoV. The signals of the SIS detectors, together with some housekeeping signals, are conditioned and multiplexed within the OH. Small footprint, precision, low-noise, low-power and Rail-to-Rail COTS (Commercial-Of-The-Shelf) operational amplifiers were selected, qualified and screened for the Front-End SIS electronics. Tests of these parts included radiation (TID, up to 30 krad) (Álvarez et al. 2014), vibration, shock, thermal cycling and operation in extreme temperature (down to -135 °C). The photodetectors and the optical elements were also tested using similar procedures.

The PE is a small processing unit that performs the analog-to-digital conversion of the signals received from the OH, plus some others internally generated at PE, stores the resulting information, and communicates with DREAMS CEU in order to control the operation of SIS and to send the resulting data packets. The unit is based on space grade parts, being its core an anti-fuse FPGA. PE offers two possible operation modes, namely Manual and Automatic. In the Manual mode, the unit is always the slave in a Master/Slave communication in which the CEU must command a new acquisition and data returning each time it wants to get some data from SIS. In the Automatic mode, the CEU commands SIS to perform automatic acquisitions of all its signals without further intervention of CEU and according to a desired sampling period form. Then SIS operates autonomously storing data on its internal memory (up to 128 kB), until it is requested to stop and dump the data to CEU, or until the memory gets full.

PE also incorporates a MEMS (Micro Electro-Mechanical System) accelerometer to determine the tilt of the lander on the surface of Mars. This is also a COTS part that was qualified and screened for use in DREAMS. Intensive tests include radiation, vibration, shock, vacuum, and thermal cycling (Álvarez et al. 2015).

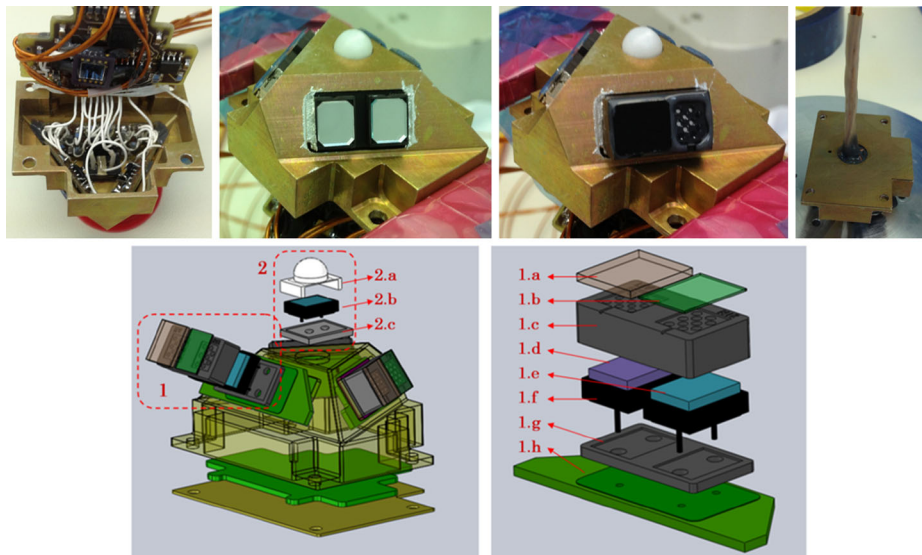


Fig. 7 Top: Views of SIS-OH during the integration process. Bottom: Detail of the Optical Head elements. 1.a, b: external UG-11 (on the UV detector) and Teflon sheet (NIR one) covers. 1.c: FoV-shaping element. 1.d,e: interference filters. 1.f: silicon photodiodes. 1.g: radiation shield (added to ensure a minimum thickness of aluminum for radiation protection). 1.h: printed circuit board with the current-to-voltage amplifiers. 2.a: diffusing dome covering the unfiltered detector. 2.b: silicon photodetector (without any filter). 2.c: radiation shield

2.7 CEU

The CEU (Central Electronic Unit) is a modular unit (Fig. 8) designed to provide all primary functionalities needed for operation, data acquisition and communication as timeline-based environmental operative sequences, analogue to digital conversion for the analogue environment sensors, power transformation and supply for all sensors/conditioners. The unit also performs data compression to meet the requirements on data volume budget for the ExoMars mission and realizes data packetization for telemetry transfer to the EDM on board computer using non-volatile mass memory for data storage.

The CEU is able to execute self-test and to provide information of status and sensors health during in flight checkouts.

The modular design is based on a plug-in configuration, splitting functionalities into different boards connected through a common backplane; the boards installed on the ExoMars 2016 flight unit are:

- OBDH Board implements the control layer of the CEU: stores and applies the Data Acquisition Timelines, interprets and forwards the telecommands coming from EDM to the peripheral boards (including data on power source use), collects the housekeeping data, acquire sensors data, stores HK and sensor data in a devoted 4 Gbit nonvolatile memory and uploads the data to the EDM for transmission to relay orbiter and then back to Earth;
- DC/DC Board performs the power distribution to lines of CEU boards and of each sensor according to the profile of each mission phase;
- CPU Board compresses high volume data with dedicated algorithms depending on specific structure of data packets. This board also incorporates all the physical layers of the interfaces towards the MicroARES board and DREAMS P/H sensor;

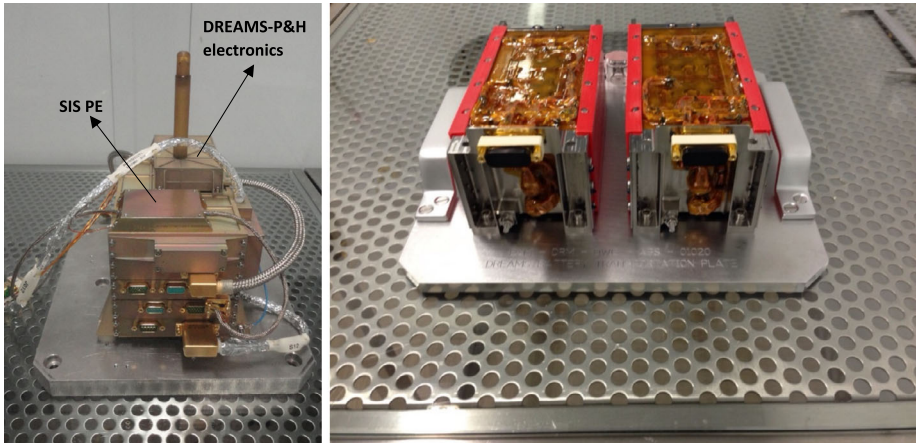


Fig. 8 Left: CEU FM; right: two models of the battery units

- MicroARES Board is integrated in a dedicated slot of CEU, and performs the control of power and data handling of the MicroARES sensor;
- ADC Board performs conditioning and acquisition of signals of analogue sensors depending on operative timelines. The data collected are transferred to the OBDH Board for storage and transmission.
- The CEU assembly hosts a relay module used to switch the power from the main bus to the DREAMS own Battery. In addition a devoted timer, which convert UTC into Mars Local time, is operative all along the scientific mission. It synchronizes the data communication from to lander electronics, and it allows the Mission Timeline execution.

Overall dimensions are 180 mm × 151 mm × 136 mm with a total mass for the complete flight model of 2219 g.

2.8 Battery

DREAMS power source for autonomous operation on Mars is a rechargeable battery (Fig. 8), based on Li-Ion rechargeable cells arranged in 8s3p lay-out, containing 3 strings in parallel, each consisting of 8 cells in series. Nominal voltage for fully charged battery is 33.6 V and an overall battery capacity of 6.9 Ah.

Charging and discharging sequences before launch are realized through a 7 pin micro connector installed on Warm Compartment connector bracket, using dedicated ground support equipment compatible with ISO 7 environment specifications. Last battery charging for DREAMS flight unit was performed on January 20th 2016 in Baikonur before closing Schiaparelli for final preparation for launch.

Overall battery envelop is 200 mm × 100 mm × 95 mm with a total mass of flight unit of 1691 g.

Mechanical structure of battery includes heaters and thermostats (nominal and redundant) to keep the battery temperature within the required temperature range (−17 °C, +50 °C), while controlling relays are mounted on a side of CEU unit and commanded through the CEU DC/DC board.

Lifetime prediction of the battery for nominal operation on Mars is around two sols taking into account charge depletion during launch preparation and cruise to Mars and the power needed for temperature control.

The DREAMS power consumption has been measured during environmental testing for all possible operational states foreseen during cruise and on Mars surface; at the nominal battery voltage of 28 V an average power consumption of 5.60 W has been measured in Cruise and Surface states, that rises to 7.84 W during acquisition, a consumption of 6.72 W in Upload state and of 0.28 W in idle state.

The DREAMS overall mass, as measured on the Flight Model, is 4362 g.

3 DREAMS Calibrations and Performances

3.1 Calibrations

DREAMS sensors have been calibrated individually by the various lead team members. The overall calibration has been then verified at the DREAMS project level.

3.1.1 DREAMS-H

Calibration of DREAMS-H has been done in similar way as calibration of REMS-H (Harri et al. 2014b). Three flight grade models, Flight (FM), Spare (FS), and Ground reference (REF), were manufactured at the same time, using parts from the same lots, and calibrated simultaneously.

Temperature calibration of Thermocap[®] sensor heads has been performed at several stable temperatures between 203 K and 333 K. The resulting accuracy of the temperature readings by Thermocap[®] is better than ± 0.1 K compared to the used reference Pt100 sensor, which in turn has calibration traceable to national standards.

For room temperature measurements, a simple humidity calibration function without temperature compensation was determined from the measurements made in several humidity points in 295 K temperature. This simple calibration function is only to be used for interpreting measurements made close to the room temperature (above 283 K), with approx. $\pm 4\%$ RH accuracy.

For low temperature (< 273 K) measurements, DREAMS-H dry (0%RH) calibration curve was established from measurements performed in vacuum in the temperature range of 203...293 K, and saturation ($\sim 100\%$ RH w.r.t. ice) curve from measurements performed in saturated air in 203...250K temperature range. These two temperature-dependent calibration curves, dry and saturation, are the basis of the nominal calibration function of DREAMS-H. To determine the response of DREAMS-H between dry and saturation points more accurately than with a simple linear fit, intermediate humidity points of approx. 30%, 60%, and 90% RH w.r.t. ice were also measured in the calibration facility of the Finnish Metrology Center (VTT) in several stable temperature points between 203 K and 263 K. To determine the response of DREAMS-H in changing humidity and temperature conditions, also measurements in varying conditions (so called "Mars sol simulation") were performed. The main calibration was done in ambient pressure, air, except for the dry curve which was done in vacuum. The CO₂ effect on Humicap capacitance was measured separately.

Indeed, CO₂ affects the capacitance of the Humicaps, the effect being larger in high pressure and cold temperature. In Martian pressure range the effect is negligible for temperatures above 263 K, but in colder cases it has to be compensated. For this, dry point curve of DREAMS-H ground reference model (REF) was measured also in 8 hPa CO₂ environment in the temperature range of 203...293 K, and compared to the curve measured in vacuum. Based on these measurements, the temperature dependent offset caused by CO₂ for the dry

curve was calculated. The offset was of the same order for all 3 Humicaps on DREAMS-H REF, and also for the Humicaps on REMS-H REF device, for which dry point comparison in vacuum and 8 hPa CO₂ was also made. The DREAMS-H Humicap capacitances measured on Mars shall be adjusted by this offset before calculating calibrated humidity values. Also wet point verification measurements with DREAMS-H and REMS-H reference models in low pressure CO₂ environment are under way.

The details of the calibration procedure will be published in a separate paper.

With the calibration based on the measurements made at FMI and Finnish Metrology Center, and using the mathematical compensation for the Humicap[®] chip lag in cold temperatures and the PTFE filter effect, the accuracy of humidity measurements in changing temperature and humidity conditions is better than $\pm 10\%$ RH in the temperature range of 203...273 K, and in order of $\pm 20\%$ RH in the temperature range of 190...203 K. In dry conditions (RH < 10%), better accuracy of $\pm 4\%$ RH over the whole operational temperature range is achieved.

3.1.2 DREAMS-P

The calibration of DREAMS-P was performed in August 2014 at FMI, in air environment. The Barocap measurement principle is based on the medium gas pushing the capacitance plates closer or further away from each other. This plates movement is not affected by CO₂. There is no polymer in this case, that would react to different gases as with Humicap sensors. In the sensor level calibration the output of the pressure sensor was measured in several pressure and temperature points under stable and under changing temperature. The stable temperature measurements were performed in the range of 0–1400 Pa (vacuum to Martian pressure range) with 100 Pa intervals and in $-45\text{ }^{\circ}\text{C}$ to $+55\text{ }^{\circ}\text{C}$ temperature (operational temperature range inside DREAMS CEU box) with max $15\text{ }^{\circ}\text{C}$ intervals. In the measurements under changing temperature, pressure was kept at 800 Pa while temperature was swept over the operational range down and up, once with as fast rate as possible, and once slower, simulating an actual sol in the mission based on thermal modeling of the CEU. A Vaisala PTB201 pressure transmitter modified for the Martian pressure range and MKS Baratron 10 Torr pressure transmitter were used as pressure references. The accuracy of the reference sensors is 0.2 Pa and their calibration is traceable to national standards. The reference temperature was measured with Pt100 sensors with calibration also traceable to national standards.

Based on results of environmental tests and experience from previous planetary missions, it was known that the pressure dependence of Barocap[®] sensor heads is extremely stable, but small changes in temperature dependence and offset may occur, especially after integrating the sensor inside the CEU. To determine these changes, calibration check was performed in vacuum at DREAMS level, after integrating DREAMS-P in CEU. Several calibration checks were also performed during the interplanetary cruise using vacuum as reference. Readings measured in the last cruise check-out were used to compensate the offset drift during storage and cruise (as reported in Sect. 3.2).

Based on the calibration checks performed at sensor and DREAMS level, it can be concluded that in general, in both transducers, Barocaps on channel 2 have better performance than Barocaps on channel 1, so they should primarily be used for scientific purposes. The total accuracy of Barocap #2 is 2.7 Pa for DREAMS-P1, and 3.2 Pa for DREAMS-P2. The repeatability, meaning maximum artificial variation on diurnal time scale (peak to peak), is 1.4 Pa for P1 and 2.5 Pa for P2, and the resolution 0.1 Pa for P1, and 0.5 Pa for P2. These performance parameters are valid after the sufficient warm-up time has passed from the powering of each oscillator (8 min for P1, 2 s for P2).

Table 1 DREAMS-P performances

Oscillator	1 DREAMS-P1 (NGM)		2 DREAMS-P2 (RSP2M)	
	1	2	1	2
Channel				
Repeatability = Maximum artificial variation on diurnal time scale (peak-to-peak)	4.3 Pa	1.4 Pa	6.5 Pa	2.5 Pa
Absolute accuracy	5.0 Pa	2.7 Pa	7.2 Pa	3.2 Pa
Resolution (peak-to-peak)	0.1 Pa	0.1 Pa	0.4 Pa	0.5 Pa
Warm-up time	6 min	8 min	2 s	2 s

Table 1 summarizes the performances of DREAMS-P.

3.1.3 MarsTEM

At sensor level the calibration of MarsTEM has been done in a thermal bath, filled with liquid ethanol, with a stability of 0.03 K and by performing a comparison between the MarsTEM and a calibrated platinum RTD whose accuracy is better than 0.05 K in the foreseen operative range. The calibration is performed in the range $-120\text{ }^{\circ}\text{C} \dots +40\text{ }^{\circ}\text{C}$. The accuracy estimation includes other effects such as the Seebeck on the junctions and soldering. Connecting wires between MarsTEM and CEU have been selected to have low Seebeck effect with platinum sensitive element.

A second step calibration was also performed at DREAMS level (both in vacuum and at 6 hPa between $-120\text{ }^{\circ}\text{C}$ and $+55\text{ }^{\circ}\text{C}$) in order to take into account the effects due to the electrical resistance of the cables and their variation versus temperature.

Final accuracy and resolution for MarsTEM are 0.1 K and 0.02 K, respectively.

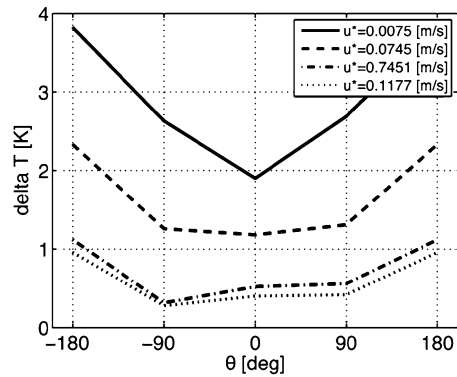
Self heating effect for the MarsTEM was considered at design level (Vidali 2012). A mathematical model of MarsTEM representing the sensitive element (platinum wire) was developed and tested with several different ambient profiles in order to choose the wire diameter, the insulation thickness, the housing material. An electrical current profile was studied in order to reduce as much as possible the self-heating with a duty cycle of 23% (15 ms ON–50 ms OFF) with a 1 mA current. The maximum increase in temperature observed was around 0.001 K (after 80 s) in a typical Martian-like environment (CO_2 atmosphere at 6 mbar). Sampling is set at 0.2 Hz.

A study was also performed in order to investigate and quantify the flow distortion due to the presence of Schiaparelli lander (MarsTEM is accommodated at about 200 mm from the deck) and MetMast shape and the temperature perturbation due to the buoyant thermal plume from the lander itself. The complete results of the thermal and Computational Fluid Dynamics (CFD) of the lander can be found in Chiodini et al. (2014).

Results of the simulation are displayed in Fig. 9, where the difference in temperature measured at the MarsTEM locations versus the incoming fluid temperature, for different wind velocities and a deck temperature of 231.5 K are shown. Thermal plume in low wind conditions led to a circulation around the lander, which modifies wind direction and speed around the lander.

The experimental verification of the flow distortion has been performed at the Martian Wind Tunnel in Aarhus (Holstein-Rathlou et al. 2014). These results will be presented in a separate paper.

Fig. 9 Difference between flow temperature at MarsTEM location and free stream. u^* is the friction speed corresponding respectively to 0.1, 1, 10 and 15 m/s incoming wind velocities



3.1.4 MetWind

The MetWind calibration included the following steps:

1. Resistance vs Temperature calibration
2. Wind tunnel calibration:
 - o Measurement of sensor output as function of wind angle (Oxford Mars wind tunnel)
 - o Measurement of sensor output in varying wind speeds (Oxford Mars wind tunnel)
 - o Measurement of the shadowing effects by the MetMast (Aarhus Mars wind tunnel)

Resistance vs Temperature Calibration MetWind sensor was subjected to a thermal soak in the temperature range of $-77\text{ }^\circ\text{C}$ to $+127\text{ }^\circ\text{C}$.

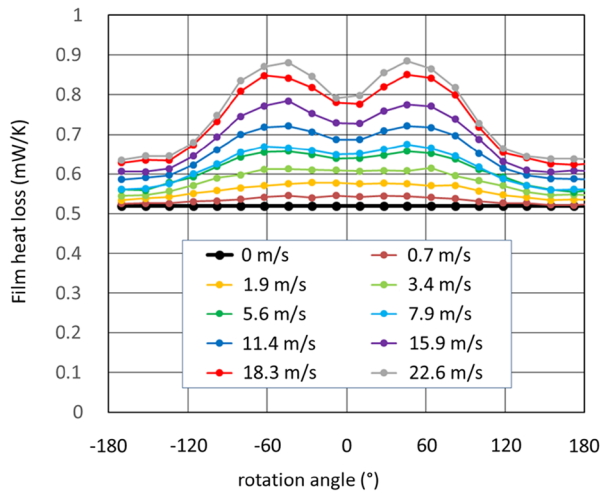
A linear fit of the form $R(T) = R_{ref}^*(1 + \alpha(T - T_{ref}))$ was found to describe the temperature dependence of resistance of each of the three platinum films. R is the film resistance, T is temperature, R_{ref} and T_{ref} are respectively the resistance and temperature of the PTR sensor (Rosemount MF0118 PRT500) used as reference, α is a calibration parameter.

Wind Tunnel Calibration The first two tests were carried out in Oxford’s Low Density Wind Tunnel facility described in Wilson et al. (2008). The MetWind sensor was placed inside the wind tunnel on the axis of a stepper motor, allowing it to be rotated around its axis of symmetry to simulate different wind directions. All tests were conducted in air at room temperature and at 6 mbar pressure. Scaling to Mars conditions is achieved by using scaling laws with non-dimensional parameters: Reynolds number Re for wind speed and Nusselt number Nu for heat transfer. Discussion of the validation of the calibration approach, demonstrating the effectiveness of the scaling laws for different gases and varying pressures, is discussed by Wilson (2003). Measurements were performed both in ‘TEMP’ and ‘WIND’ modes with the sensor placed at different angles with respect to the wind direction and at different wind speeds (including no wind). Measurements were obtained by averaging measurements acquired while rotating the sensor from 0° to 360° and vice versa in order to correct for any hysteresis associated with lag in the response of the sensor to changing wind direction.

Sample results for the MetWind flight model are shown in Fig. 10.

Each curve shows data for one of the three films (averaged results from one clockwise and counter-clockwise rotations). The y axis expresses sensor performance as a heat transfer coefficient $C_{film} = q_{film}/(T_{film} - T_{air})$, where q_{film} and T_{film} represent respectively the heat dissipation (in mW) and temperature (in K) of the hot film.

Fig. 10 Calibration data for one of the MetWind Flight Model sensor films. The y-axis shows the film’s heat transfer coefficient, defined as [power dissipation/(film temperature—air temperature)]. Rotation Angle denotes wind direction, with 0° signifying that film 1 is pointing directly into the wind. Velocities have been scaled to show equivalent velocities in carbon dioxide at a temperature of 250 K and a pressure of 6 mbar



The convective part of the heat loss from each film is calculated simply by subtracting the heat flow experienced when no wind is present $C_{conv} = C_{total} - C_{(u=0)}$. This convective heat transfer coefficient is then converted to a dimensionless Nusselt number $Nu = Cd/Ak$, where d and A represent the diameter and area of the film, and k represents the thermal conductivity of the atmosphere. Finally, the baseline data analysis method uses the differences between the films to calculate wind speeds. From this we calculate an effective Nusselt vector (Nu_x, Nu_y) from which a 2D wind vector is then calculated as described in Wilson (2003).

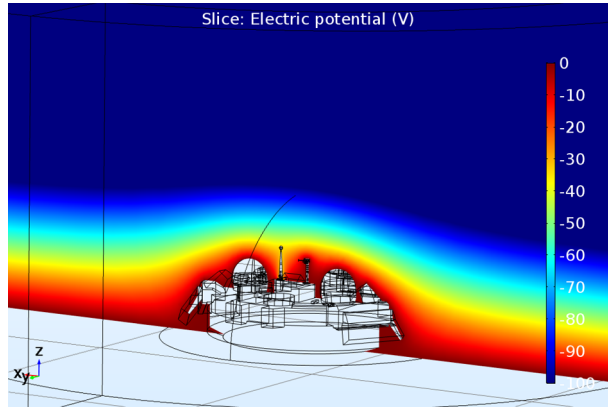
The possible shadowing of MetWind by the full assembled MetMast structure was investigated in the Aarhus Martian wind tunnel in Aarhus. Results will be reported in a separate paper.

The calibration of the MetWind sensor is prone to some of the same issues common to all thermal anemometers: the films respond not just to changes in wind speed but to all thermal loads. Uncertainties in the exact thermal environment around the MetWind sensor on Mars, due for example to changing temperatures of lander structure near MetWind, would have resulted in significant uncertainties in the absolute calibration of MetWind. If one side of the wind sensor was heated by proximity to a hot portion of the lander, for example, that would produce the same response in MetWind as a wind blowing toward that direction; such asymmetrical thermal loads could cause errors of up to 4 m/s in the measured wind vector in extreme cases, and up to 1 m/s in nominal cases. Ultrasonic time-of-flight wind sensors, as used for turbulence study on Earth, would provide a more robust calibration and faster response time (10 Hz compared to 0.2–0.5 Hz for MetWind). But MetWind proved well suited for the DREAMS goals of providing a basic landing site climatology and first-order turbulence characterization in an extremely compact and robust form.

3.1.5 MicroARES

Given that MicroARES measures the potential of its electrode, the electric field values are derived from finite element modelling of the antenna and lander immersed in an atmosphere of conductivity σ_{atm} . The model discretises the generalized Ohm law, volume charge conservation and first Maxwell law equations ($\vec{E} = \sigma_{atm} \cdot \vec{J}$; $\partial\rho/\partial t + \vec{\nabla} \cdot \vec{J} = 0$; $\vec{\nabla} \cdot \vec{E} = -\Delta V = \rho/\epsilon_0$) in order to properly simulate both the electric field deformations around the

Fig. 11 Electric field (-100 V/m vertically constant) perturbations induced by the lander. The atmospheric conductivity is 2 pS/m and the resulting electrode potential measured by Micro-ARES is $\sim 33.96 \text{ V}$. The simulations are performed with the finite-element computation software COMSOL



instrument and the resulting current collected by the electrode. The parasitic input values of the instrument (detailed below) are included in the simulation. Typical model outputs are shown in Fig. 11.

In the calibration process (Déprez 2016), signals are always injected in the instrument through so-called *injection* boxes supposed to reproduce the coupling of the electrode with the atmosphere (Bertheliet et al. 2000). These boxes consist of a set of resistances and capacitors mounted in parallel and specified to have resistance and capacitance values close to conditions relevant for the Micro-ARES electrode when immersed in a Martian-like atmosphere.

To calibrate the various components of the instrument part, potential is measured at various test points and the necessary relations (linearity, gain or frequency response) are subsequently established. The measurement uncertainties are given in the datasheets of the various devices. However, when the test point of the instrument measurement is used (in Least Significant Bits, LSB) the value and error are respectively derived from the average and standard deviation of a measurement set. The uncertainties are then propagated by fitting the data with adequate functions, using the least-square method to take into account the uncertainties of all inputs.

DC Channel The DC chain was calibrated during Thermal vacuum tests, with temperatures ranging from $45 \text{ }^\circ\text{C}$ to $-35 \text{ }^\circ\text{C}$ (every $5 \text{ }^\circ\text{C}$). The DC linearity at each temperature with each Injection box and at 17 steps was measured between -80 V and $+80 \text{ V}$.

The electronic chain is described by equation (Millman theorem) shown below, which is fitted with data gathered during the TVT using the least-square method, in order to properly propagate the uncertainties:

$$V_{injected}(LSB, T, Re) = V_{mes}(LSB, T) \cdot \left(1 + \frac{Re}{Ri(T)} \right) - i_L(T) \cdot Re$$

$$Ri(T) = p_4 + p_5 \cdot T$$

$$i_L(T) = p_6 \cdot \exp(p_7 \cdot T)$$

The resulting error on the computed electrode potential at $20 \text{ }^\circ\text{C}$ is shown in Fig. 12.

AC Channel The AC channel calibration has been performed only at $20 \text{ }^\circ\text{C}$, since the noise conditions and access to the instrument board during the TVT was limited.

Fig. 12 Error on the retrieved electrode potential at 20 °C

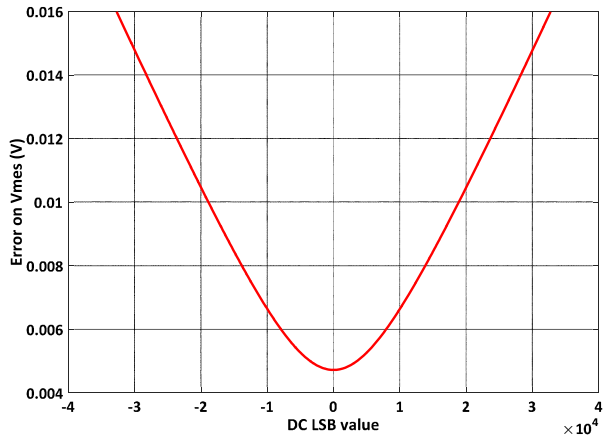
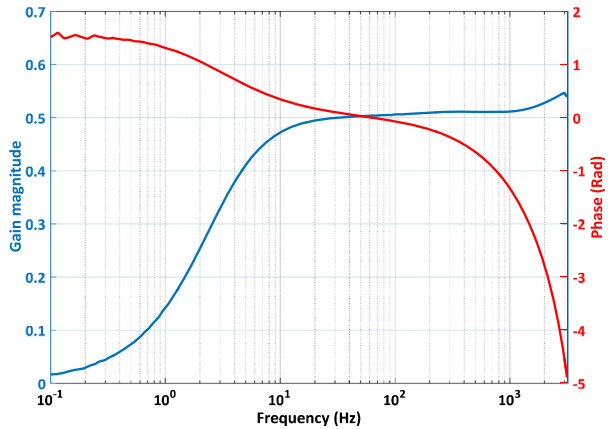


Fig. 13 AC channel response in gain and phase



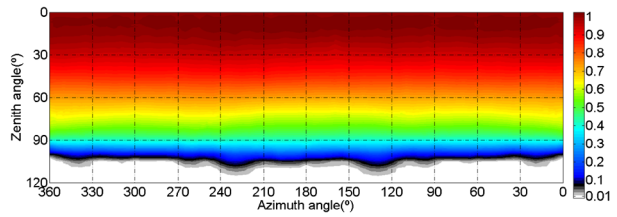
Calibration consisted in measuring the frequency response, both in gain and phase, of the whole electronic circuit (Fig. 13).

3.1.6 SIS

The calibration of SIS photodetectors consists of various steps. The first step is aimed at determining the responsivity to light normally incident to each detector. Then the variation of this response as the angle of incidence of light varies is measured to calibrate the angular response of each detector. Finally, the thermal dependence of the responsivity is measured, although the thermal effects were found to be very small.

The facilities used for this calibration are at INTA’s SPASOLAB (Space Solar Cell Test Laboratory, an official laboratory for solar cells testing according to ESA required standards). SPASOLAB has several sun simulators and Xenon lamps. A triple light source Sun simulator set to AM0 (Air Mass 0, i.e. outside the atmosphere) spectrum and a set of neutral filters are used for the normal-incidence responsivity calibration. For the angular dependence, SIS OH is mounted on a rotating mechanism controlled by two high-precision (0.01° step) motors that allows the relative azimuth and zenith angle between OH and the light

Fig. 14 Angular dependence of the zenith-pointing SIS detector responsivity



source direction to be controlled. The thermal calibration is done in a thermal chamber with an optical quartz window. The accuracy of the lamp irradiance is known within $\pm 1\%$.

The dynamic range of the 3 different spectral channels is 1050 W/m^2 for the unfiltered (zenith-pointing) detector, 390 W/m^2 for the NIR detectors, and 110 W/m^2 for the UV ones. The responsivities are $0.544 \mu\text{A}/(\text{W/m}^2)$ for the unfiltered, around $1.38 \mu\text{A}/(\text{W/m}^2)$ for the NIR detectors (with slight differences between them), and $0.202 \mu\text{A}/(\text{W/m}^2)$ for UV, with minor differences between the 3 UV detectors. The uncertainty (standard deviation) in the determination of these values ranges from 0.17% to 0.41%, depending on the detector.

For the calibration of the angular dependence, the main source of uncertainty was due to the set-up itself. An error in the knowledge of the real angle of incidence of light of up to 0.5 degrees is assumed. This leads to errors in the accuracy of the angular dependence calibration of less than 5% for ± 30 degrees from the normal incidence. These errors rise up to 20% in the limit of the FoV, where the responsivity is less than 5% of that at normal incidence. Details can be found in Jiménez et al. (2016).

Thermal effects are small on SIS measurements, and become negligible after applying corrective factors as a function of the internal PT1000 sensor installed inside the OH.

Finally, it is worth mentioning the small angular dependence of the unfiltered, zenith-pointed, detector. Its angular dependence shows revolution symmetry when varying azimuth, and regarding zenith angle, the responsivity is still higher than 90% of the normal incidence one for 35 degrees. It is still 80% of the normal incidence responsivity for a zenith angle of 50 degrees, whereas the total average responsivity is 81% of that for normal incidence, when its complete hemispherical FoV is considered. Thanks to this, to convert the measured photocurrent (A) into irradiance (W/m^2), a direct application of the normal incidence responsivity value is possible, with acceptable error, regardless of the particular Sun position. Specially, if the Sun is in a low relative zenith angle, the direct, circumsolar, and most of the diffuse light will actually be received with a responsivity very close to the nominal (normal incidence) value, making the estimation of the absolute irradiance a very straightforward process. Figure 14, extracted from Jiménez et al. (2016), shows this angular dependence:

The performances of all SIS detectors are summarized in Table 2. During the trip to Mars, the accumulated radiation will degrade the detectors' responsivity in a different amount for each spectral band. Radiation analysis shows that the maximum signal degradation for the expected radiation levels (margins accounted) is 14% (for the NIR sensor which is the worst case). This can then be reduced thanks to the estimation of the Displacement Damage suffered by the detectors, obtained through the monitoring of the dark-current of the reference detector included for this purpose.

The calibration of the accelerometer inside the PE was done using precision motors and precision bubbles to fix the horizontal position for each axes. First the real orientation of each axis with regard to the PE box was found, and then rotations around the axis were applied in order to find the offset and sensitivity of each accelerometer. Only X and Y axes were acquired, allowing for a complete determination of the tilt angle of the XY plane after landing, and rotation of the X and Y axis within that plane. Different analysis were

Table 2 SIS performances as computed from calibration. Note: It must not be surprising that the indicated values in the table, even the noise, depend on the angle of incidence of the light. This is because the different magnitudes have been expressed as an equivalent irradiance. But to translate, for example, a noise, into irradiance, the sensor's calibration equation must be used. This equation includes an important parameter which is the Angular Response Function of the sensor, that depends on the angle of incidence of the light. For that reason the "equivalent irradiance" of that noise depends on the angle we may suppose in a hypothetical scenario

Incident light angle		Noise, expressed as equivalent irradiance [W/m ²]	Accuracy ^a		Precision	
			Value	Unit	Value	Unit
TOP	@ Normal incidence	1.1×10^{-3}	1	%	0.04	%
	@ 50% of the FoV	2.2×10^{-3}	3	%	0.1	%
	Under diffuse light	1.4×10^{-3}	1	%	0.003	W/m ²
NIR	@ Normal incident	0.4×10^{-3}	1	%	0.004	%
	@ 50% of the FoV	0.8×10^{-3}	6	%	0.08	%
	@ 10% of the FoV	4×10^{-3}	10	%	0.4	%
	Under diffuse light	0.5×10^{-3}	1	%	0.005	W/m ²
UV	@ Normal incident	0.1×10^{-3}	2	%	0.04	%
	@ 50% of the FoV	0.2×10^{-3}	7	%	0.1	%
	@ 10% of the FoV	1×10^{-3}	10	%	0.4	%
	Under diffuse light	0.12×10^{-3}	1	%	0.001	W/m ²

^aIt is supposed a solar position accuracy of 1 deg

carried out to find the uncertainty that could be introduced by thermal effects and by the uncertainty in the knowledge of the gravity of Mars (which affects the calculation of the XY rotation within its plane). It was found that the required uncertainties in the temperature and gravity knowledge, needed to create a tilt uncertainty of 1°, were around 12 °C and 1.5 m/s² respectively. The thermal effects were however calibrated by using a thermal chamber and some fixed inclinations provided by special support tools. The knowledge of gravity is better than ± 0.05 m/s².

The acquisition scheme of SIS makes use of an oversampling acquisition that provided around 20 bits of free-of-noise effective resolution for the photodetecting channels, as measured during the calibration campaign.

Finally, it is worth noting that, in a long-duration mission, dust deposition on the detectors surfaces will be the main source of degradation of the total responsivity. The use of magnets around the photodetectors, to slightly deflect the dust trajectory and thus minimize its deposition rate, was proposed for the Rover Environmental Monitoring Station (REMS) on Curiosity (Smith et al. 2016). The same is being done in the Radiation and Dust Sensor (RDS) of MEDA, the next-generation meteorological station that INTA develops for the Mars2020 Rover (Apéstigue et al. 2015). Also, the responsivity degradation can be roughly estimated through the analysis of the yearly evolution of all the sensors lying in the same plane (a number of sensors, all of them showing similar long-term signal decrease), as experienced in REMS.

Nevertheless, for all scientific retrieval algorithms for which relative instead of absolute signals are employed (i.e. the ratio between the signals delivered by detectors in different sides of the optical head), an in-situ calibration process is proposed. It is worth noting that the estimation of the optical depth can be done by means of these purely differential measurements. The method consists in comparing the signals provided by each couple of de-

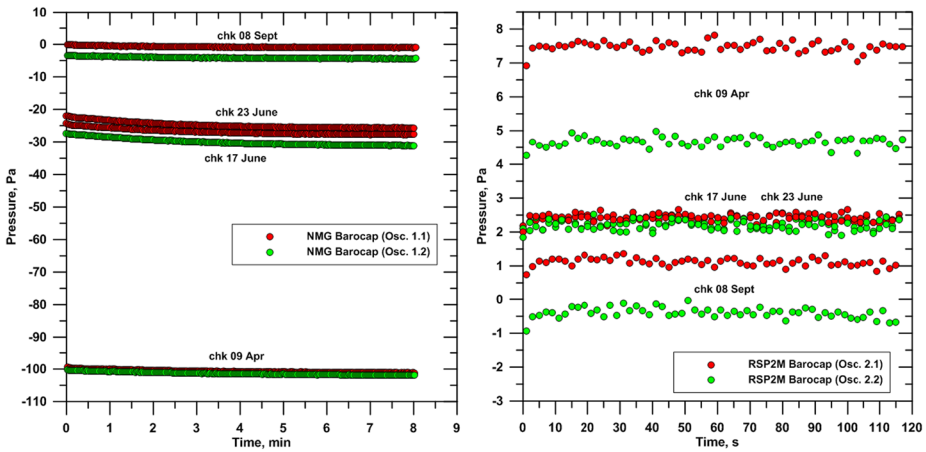


Fig. 15 DREAMS-P pressure reading during the cruise checkouts on 9th April, 17th, 23rd June and 8th September, respectively. Readings from channel 1 of each pressure sensor are represented in red, while green indicates data from channel 2. P1 sensor (left plot) shows untypical behaviour going from -100 Pa reading at the first checkout to about 0 Pa in September. Note that P1 sensor has no space flight heritage. P2 sensor behavior is as expected

tectors when the Sun lies in a symmetric position with regard to their FoVs. In the absence of degradation, each detector should generate the same signal (within their initial differences in responsivity). This technique also allows, during the first Sols of a mission (when dust deposition is still negligible) to determine the orientation of the sensor after landing, as was demonstrated during the field campaign carried out in the Sahara desert (Arruego et al. 2017).

3.1.7 DREAMS Performances

The performances of DREAMS sensors are summarized in Table 3.

3.2 In-flight Performances

During the trip to Mars all the DREAMS sensors were activated for calibration and health check tests. Sensors have been activated for three nominal and two additional checkouts between April and September 2016. All sensors performed nominally.

During the cruise, Schiaparelli was encapsulated inside the spacecraft rear and front shields. Vacuum and dry conditions were expected inside the spacecraft. Thus, the readings from DREAMS-P and DREAMS-H have been used to correct on-ground calibration for the natural drifting of sensors and other effects. Figure 15 shows the trend of P1 and P2 sensors readings during the various checkouts. As expected, both sensors experienced outgassing during the cruise. The trend of P1 sensor resulted untypical but both sensors resulted completely outgassed and with reading of few Pa about one month before the landing.

DREAMS-H offset was also measured during all the checkouts.

In the last checkout before landing phase it was between -2.4% and -1.5% depending on Humicap sensor (Fig. 16).

MarsTEM behavior was nominal (Fig. 17).

Table 3 Performances of the DREAMS sensors

Sensor	Measured Quantity	Range	Resolution	Accuracy
MarsTEM	Temperature	70–320 K	0.02 K	0.1 K
DREAMS-P	Pressure	0–1015 hPa	< 0.5 Pa	< 5 Pa (BOL) ^a
DREAMS-H	Relative humidity	0–100%	0.5% RH	±10% RH down to –70 °C ±20% RH down to –83 °C +/-4% RH in dry conditions at all T
MetWind	Wind speed Wind direction	0.3–30 m/s and above	0.1 m/s	+/-1 m/s +/-10° for wind speeds > 5 m/s
MicroARES	Vertical Electric Field and potential	<i>DC channel</i> –256 to +256 V/m in native mode > 10 kV/m in HV mode, depending on the atmospheric conductivity <i>AC channel</i> 4–3200 Hz frequency range 15 V/m peak-to-peak in standard mode 0.2 V/m peak-to-peak in high sensitivity mode	<i>DC channel</i> 8 mV/m in native mode ~ 0.1 V/m in HV mode, depending on the atmospheric conductivity <i>AC channel</i> 0.26, 0.52 and 25 Hz spectral resolution in the respective 4–50, 50–100 and 100–3200 Hz bands 0.2 mV/m in standard mode 3 µV/m in high sensitivity mode	<i>DC channel</i> 60 mV/m in native mode ~ 1.2 V/m in HV mode <i>AC channel</i> 0.15 mV/m in standard mode 2 µV/m in high sensitivity mode
SIS		<i>Under direct normal light</i>	<i>Under direct normal light</i>	<i>Depends on the angle of incidence of the light</i>
	Solar Irradiance	Tot: 220–1200 nm: 0–1050 W/m ²	TOP: 1 mW/m ²	Tot. irradi.: 1–30% (30% for SZA > 85 deg)
	Dust opacity	NIR: 700–1100 nm: 0–390 W/m ²	NIR: 0.4 mW/m ²	NIR: 1–10%
	UV intensity	UVA: 315–400 nm: 0–110 W/m ²	UV: 0.1 mW/m ²	UV: 1–10%

^aThe reported value of the accuracy of the pressure sensor refers to channel 2 of both DREAMS-P1 and DREAMS-P2 sensors (see Sect. 3.1.2)

MetWind was turned on several times during cruise. Figure 18 shows the evolution of film temperatures during the last in-cruise check-out, on September 2016. The plot shows the temperatures of the hot films and of the housekeeping temperature sensor located in

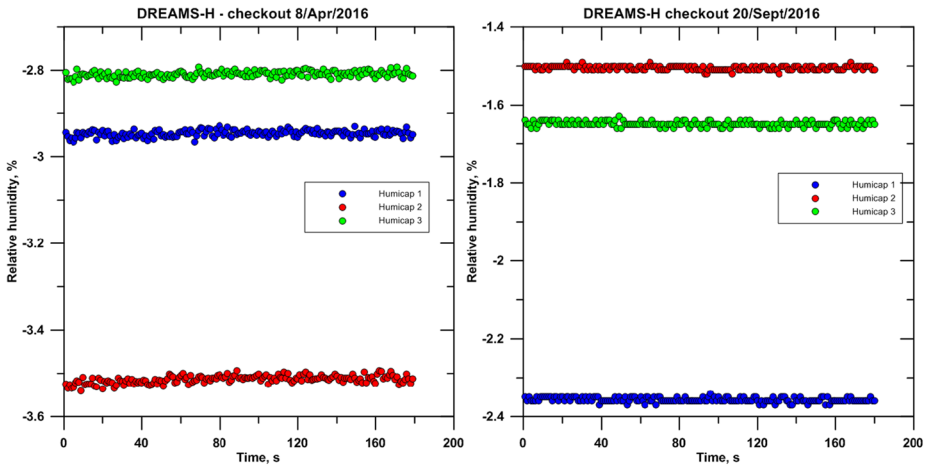
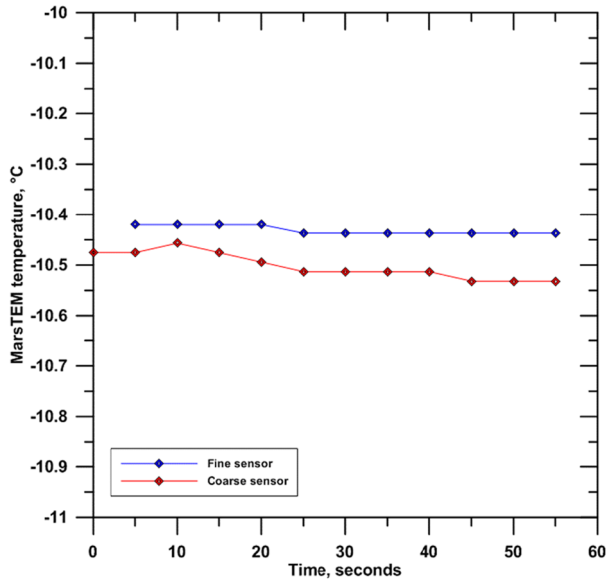


Fig. 16 DREAMS-H reading during the first (left) and last (right) checkout

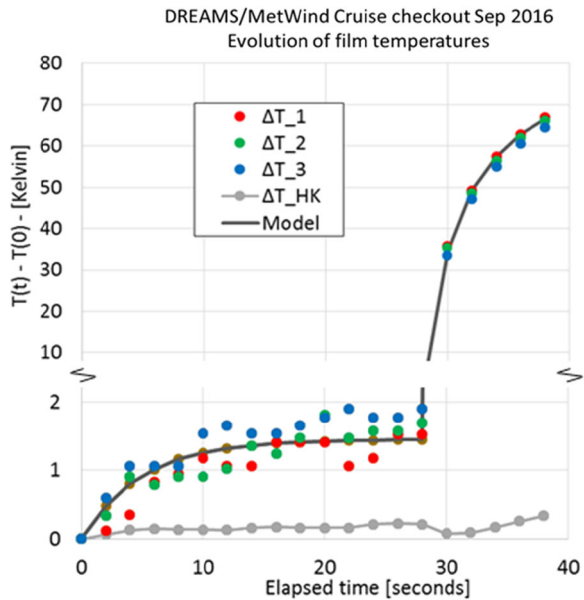
Fig. 17 MarsTEM signal as acquired during the June checkout



the centre of the MetWind sensor, as described in Sect. 2.4. During the first 30 seconds, the sensor was in its low power mode where only ~ 2 mW are dissipated in the films. After 30 seconds MetWind was switched into its wind sensing mode, where ~ 40 mW are dissipated in the films, to check the correct functioning of its electronics. This high power mode was used only for ten seconds to avoid overheating of the films, a condition which can arise in the vacuum of space when the films are not convectively cooled. The behavior of the wind sensor in these tests was nominal.

MicroARES health check produced also expected results in terms of housekeeping values and sensor behavior.

Fig. 18 MetWind film temperatures during the last in-flight checkout, in Sep 2016. Heating power in the films was ~ 2 mW for the first 30 seconds, 40 mW for the subsequent 10 seconds. Note the discontinuity in the vertical scale. ΔT_{HK} refers to a housekeeping temperature, measured at the centre of the MetWind sensor



SIS confirmed the excellent quality of the signals. Figure 19 shows some of the telemetry acquired during the last activation before reaching Mars.

As it can be seen, the noise in the UV photodetectors show a standard deviation equivalent (when converted to irradiance) to around 0.1 mW/m^2 , which compared to the 110 W/m^2 dynamic range equals 0.9×10^{-6} (i.e. more than 20 bits of free-of-noise resolution). The noisiest channel, due to the high gain employed in the current-to-voltage conversion, was the dark-current one. For this channel, the requirement was to measure from pA to almost 40 nA (which would be equivalent to more than 15 bits of free-of-noise resolution). The telemetry shows that the pA resolution was actually achieved.

The DREAMS in-flight data are archived into the European Space Agency's Planetary Science Archive (Schipani et al. 2016). The archive adopts the NASA's Planetary Data System version 4 (PDS4) standards as a baseline for the formatting and structure of all data.

4 Test in the Sahara Desert

DREAMS was fabricated to land on Mars during the dust storm season. For this reason, the instrument has been designed to cope with a dusty environment. The landing during the dust storm season would also provide a great opportunity to study, for the first time, the effect of dust on the electric properties of the Martian atmosphere.

Field experiments have been performed in the Sahara desert in 2013 and 2014, during the dust storm season, to test sensor response to harsh environment and study the relation between the emission of dust and the electric properties of the atmosphere. The results of these tests are a good start point to understand the dusty environment of Mars from future DREAMS acquired data.

The scientific goal of the field campaign was the study of the development and evolution of dust storms and dust devils. For this aim, a meteorological station (see Fig. 20), particularly devoted to the monitoring of sand saltation process (the bouncing of sand grains

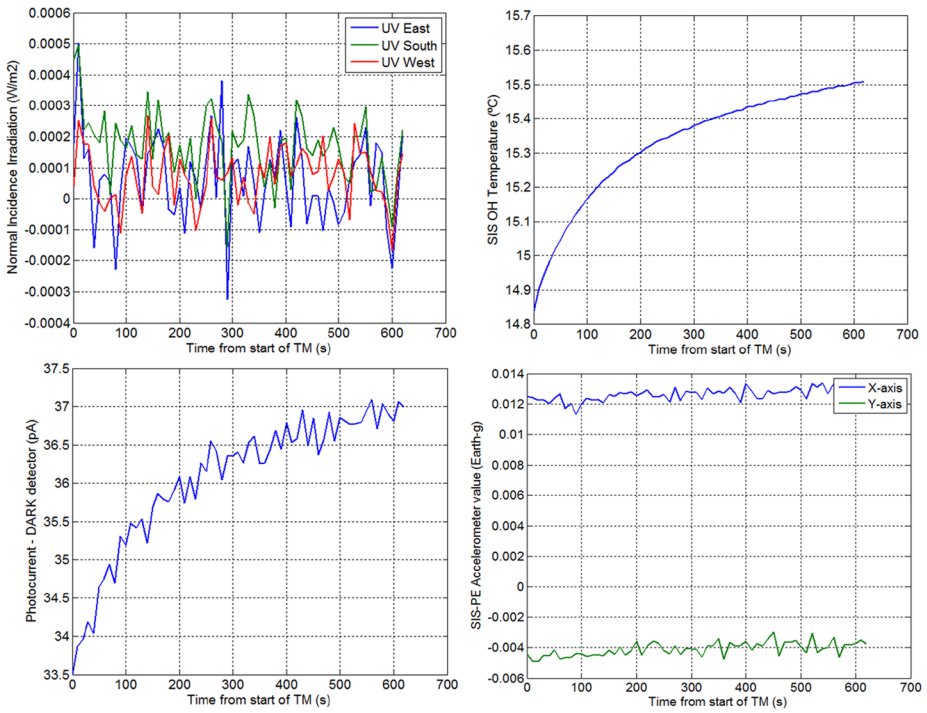
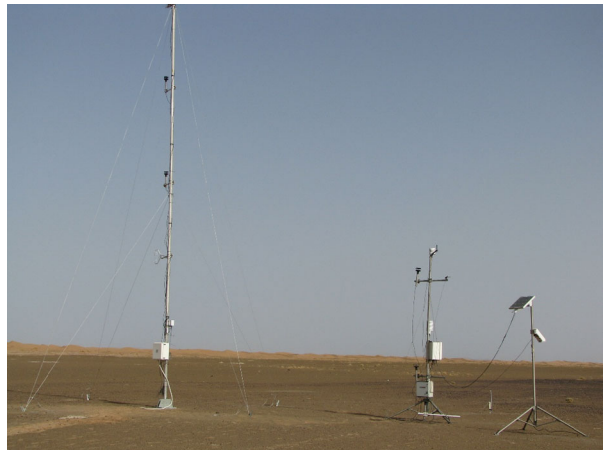


Fig. 19 Some telemetry from the SIS activation on September 21st. From top to bottom and left to right: signals from the UV detectors expressed as the equivalent normal-incidence irradiance that would be necessary to generate the measured photocurrents, OH temperature, Dark current of the reference dark detector, and accelerometers signals

Fig. 20 Meteorological station deployed in the Sahara desert for the study of dust lifting process and its feedback on the electrical properties of the atmosphere



above the soil when blown by the wind) and dust entrainment in the atmosphere, has been deployed in the region around Merzouga (Errachidia) in the Moroccan desert. This desert has a Martian-like terrain and offers a good chance to understand the physics behind aeolian

processes. The chosen area is particularly rich in both sand and dust particles and it is very active from the aeolian point of view.

The following physical quantities have been monitored for six months during the Summers 2013 and 2014: wind speed and direction at six different altitudes (wind vertical profile), atmospheric humidity, temperature at two heights, pressure, solar irradiance, soil moisture and temperature, sand saltation rate (by detecting the impacts of sand particles over two impact sensors), atmospheric electric field (Campbell CS110) and the size distribution and number density of dust grains entering into the atmosphere. The goal was to correlate environmental parameters to sand movements and dust entrainment and, in particular, verify the effect of sand saltation process on the generation/enhancement of the atmospheric electric field. Data analysis shows that charging of grains during aeolian processes produces an enhancement of the atmospheric electric field. E-fields up to 20 kV/m have been observed during the most intense dust storms. Note that the fair weather field is of the order of 50–100 V/m. The field intensity results to be linearly related to the number of lifted grains and negatively correlated with relative humidity. Moreover, data indicate that strong E-fields are also capable to enhance dust lifting in a feedback process. A detailed discussion of campaign results is reported in Esposito et al. (2016). Similar data could be collected by DREAMS instrument on Mars.

During July 2014, some of the DREAMS sensors, MicroARES, MarsTEM and SIS, were added to the meteorological station deployed in the desert (Fig. 21). The goal was to test their behavior during dusty events.

We used a terrestrial version of MicroARES antenna that was larger than the original one (Fig. 21a). This was due to the different electric conductivity on Earth and Mars. For atmospheric conductivity roughly 100 times smaller than that of Mars, an electrode roughly 100 times larger is needed in order to keep the sheath resistance R_s at the same order of magnitude. A greater R_s would cause the electrode not to be able to maintain itself at the floating local potential because of the small bias current flow to the input amplifier. The terrestrial model was a 60 cm side copper cube. Its 2.16 m² surface area was equivalent to a 41.6 cm radius sphere, around 30 times larger than the original antenna. For more details see Harrison et al. (2016).

Given the fact that the Campbell CS110 electric field mill mounted on the meteorological station can only measure electric field signals with a frequency below 0.5 Hz, only the DC data can be compared to MicroARES sensor. However, the two instruments were located 50 meters apart, with a setup at 2 meters from the ground for the CS110, and a setup at 50 cm from the ground for MicroARES. Therefore, a meaningful comparison can only remain at a qualitative level.

The ability of Micro-ARES to provide interesting data is confirmed by the concomitant dust devil detection made by the two instruments on many occasions (one example is shown in Fig. 22). The signatures of the dust devil exhibit expected differences but overall provide excellent agreement with regard to the shape and timing of the sudden electric field rises and demises.

Two prototypes of the MarsTEM sensor were tested and compared during three days of measurements: a Titanium sensor structure with an aluminium shield and a free-shield sensor with a more complex structure made with Titanium alloy and peek rods (Fig. 21b). Several reference sensors (PT100) were positioned on the upper and lower part of the shield for comparison. During the testing the weather was variable, clouds were observed both in daytime and in night-time, wind changed both in velocity and direction and relative humidity changed in the range (0...+50%). Some rainy events occurred lasting around half an hour, and some very weak dust storms were detected by the instruments. Temperature data were sampled at a 1 Hz frequency.

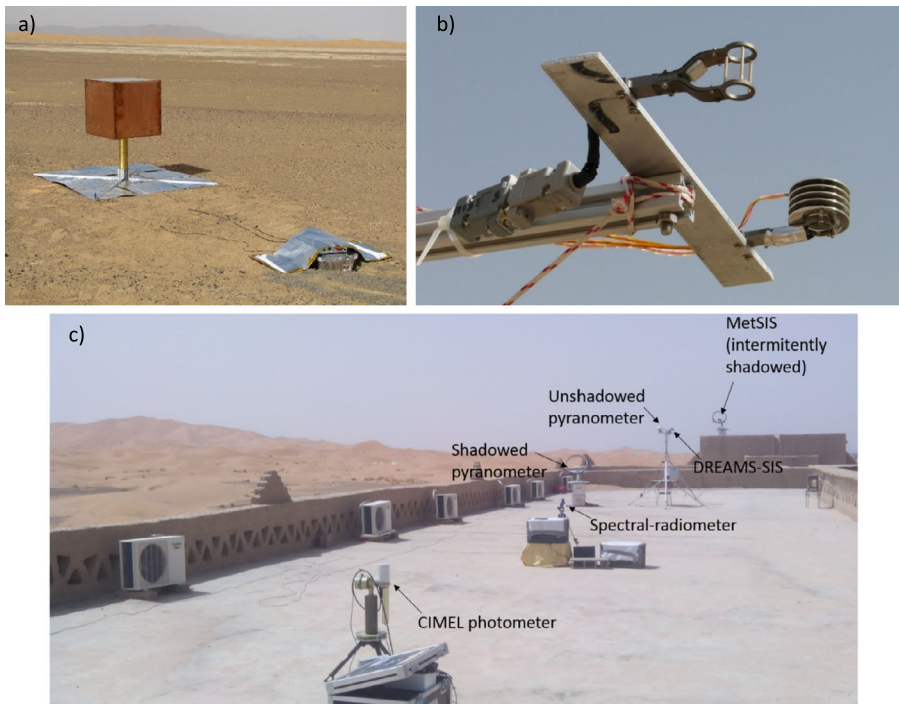


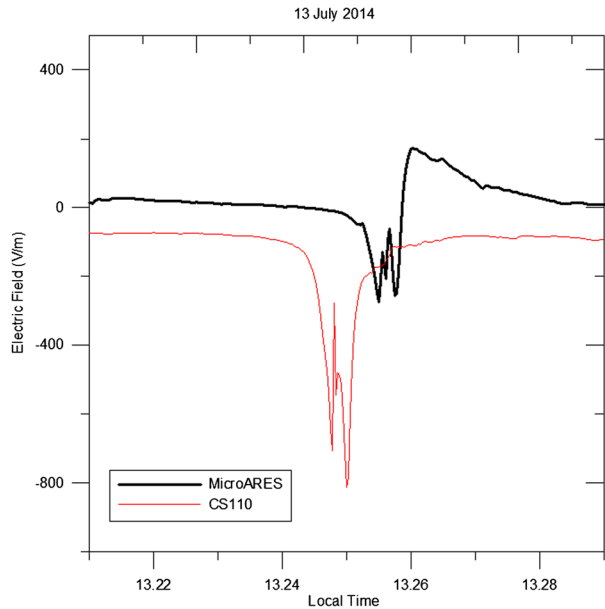
Fig. 21 DREAMS sensors added to the meteorological station deployed in the Moroccan desert: **(a)** Terrestrial version of MicroARES; **(b)** At the top: the MarsTEM temperature sensor without the radiation shield; on the bottom right: the MarsTEM sensor protected by the aluminium shield; on top, fixed to the shield, the PT100 B sensor and in the shadow of the shield the PT100 A, directly exposed to air; **(c)** SIS and other devices

Daytime data showed clearly that the aluminium shield heated up and the temperature measured by the MarsTEM sensor was affected by a non negligible bias. For this reason, and because of similar effect foreseen by an ad hoc developed simulation using a CFD code in a Martian environment (see Chiodini et al. 2015), it was decided to not equip the MarsTEM with the aluminium protecting shield.

During the nights, measurements were conducted continuously and data registered on the data logger; several peculiar events were observed and analysed (see Colombatti et al. 2015). Evidence of a strong correlation of temperature, wind (both for velocity and direction), humidity and topography was highlighted.

A test campaign was also carried out with SIS (Fig. 21c). Different procedures for estimating the atmospheric optical depth (OD) were applied. One of them is based on fitting the measured photocurrents to the expected ones according to simulations made with radiative transfer models for different atmospheric conditions. The second, is based on the same fitting but working with signals (and model estimations) normalized to their own maximum, i.e., paying attention to the shape of the signals but not to their absolute values (thus rendering negligible any possible dust accumulation effect). The last procedure compares the photocurrents generated, at each moment, by the one of the three equal lateral detectors that has the Sun inside its FoV, and the sum of the two others. In other words, it compares global (direct plus diffuse) and diffuse light. The three procedures are detailed in Arruego et al. (2017), whereas the radiative-transfer model employed to simulate the SIS signals is

Fig. 22 Dust-devil cross detection by CS110 electric field mill and Micro-ARES



described in Toledo et al. (2017). From the set of OD estimations obtained with the three different methods outlined, and with the different lateral detectors (a fitting between each detector's signal and the model, was done), the standard deviation of the estimations was found to be less than 18%.

Regarding the absolute irradiance measured with the zenith-pointing detector, it was compared to that provided by a set of two pyranometers (un-shadowed one for global light measurement, and shadowed one for diffuse light measurement). The difference between the two estimations (SIS and pyranometers) was well below 10% for solar zenith angles (SZA) as high as 50° (Arruego et al. 2017).

All tests confirm that DREAMS sensors perform nominally in harsh environment and are absolutely well suited for the monitoring of environmental parameters during dust events.

5 Operations

Surface Operation Timeline DREAMS lifetime is limited by the capacity of its power unit and the power profile during operations. The acquisition sequence was designed as a compromise among scientific goals, available energy and communication constraints due to the sequence of orbiters passages over the landing site.

In order to cope with the science goals, measurements sequence has been built in order to:

- Be almost periodic all along the day and night time. This allows to monitor the diurnal cycle of atmospheric parameters.
- Make them more frequent in the daytime and longer at midday. Indeed, the Martian climate database (<http://www-mars.lmd.jussieu.fr/>) predicts a peak in surface temperature around 13:00 Mars local true solar time (LTST) in the landing site and period (Bertrand

et al. 2016). Most of the convective activity, like high-frequency fluctuations of atmospheric wind, temperature, pressure, is expected roughly between 11:00 and 15:00. This is the most favorable period to get stronger winds and dust events (devils, storms).

- Have a long duration measurement at twilight in order to capture the highest relative humidity of the night (at sunset) and study cloud properties.

To fulfill the scientific objectives DREAMS is able to control each sensor independently, setting the start and stop time of each acquisition sequence, the acquisition rate and other parameters needed to configure the internal sensors (namely Sensor SWitch sequence: SSW). The unit is able to store in its non-volatile memory six different operation timelines. Each timeline is a list of SSW sequences to be executed in different phases of the mission. Two fail-safe mission timelines are hard-coded in the application software and cannot be changed, while the other four timelines are used for the nominal mission and can be uploaded to the unit during the interplanetary cruise to Mars. One of them is used to support the in-flight checkout operations. The other three timelines are used to implement the surface phase of the mission, they are called MTL1, MTL2 and MTL3 for convenience. Each timeline covers the acquisitions foreseen during one Martian sol starting from the local midnight. The acquisition sequences are triggered with respect to the Mars LTST computed at the center of the landing ellipse. In this way the acquisitions are correlated with the local events e.g. sunrise, sunset and specific part of the sol.

DREAMS is designed to operate autonomously once on the Mars surface. After the touch-down the descent module powers-on DREAMS, provides the mission time to the unit and then sets DREAMS in surface mode. Once in surface mode DREAMS starts executing the MTL1, then MTL2 and MTL3. At the beginning of the fourth sol DREAMS will execute again the stored MTLs starting from MTL1 and so on until the depletion of its internal battery. Acquired data is stored in the non-volatile memory of the unit waiting for the upload to the descent module. To save energy both DREAMS and the descent module are able to enter a low-power mode. The two units are kept synchronized with their internal timers and wake-up simultaneously. At each wake-up DREAMS uploads data to the descent module, then the descent module uploads data to the orbiters, notifies to DREAMS the time of the next communication window and enters hibernation again.

The design and validation of the three surface mission timelines is a crucial step for the success of the mission. These timelines are designed to satisfy several conditions listed below:

- Guarantee at least 2 sols of operation
- Max energy consumption of 120 Wh with 5% margin at the last data upload
- Acquisition and storage of at least 50 Mbit of data for each sol
- Guarantee that DREAMS is ready to wake-up when expected by the descent module (with no more than 500 ms of margin)
- Guarantee that during the communication with the descent module, MicroARES is off to avoid disturbing the UHF link with the orbiters.

The final timeline is then tested simulating a two sols mission on the DREAMS Flight Spare model.

The final surface mission timelines uploaded to DREAMS are depicted in Fig. 23. The touch down was expected on 2016-10-19 at 14:48:17. Some seconds after the touch down the initialization of the DREAMS takes place and the first hibernation cycle begins. The first SSW to be executed is the SSW #19 of the MTL #1 (first sol of operation). The nominal mission foresees the execution of 43 SSWs listed in Table 4. These SSW correspond to about 11 hours and 20 minutes of data acquisition over 51 hours and 48 minutes of operation (see

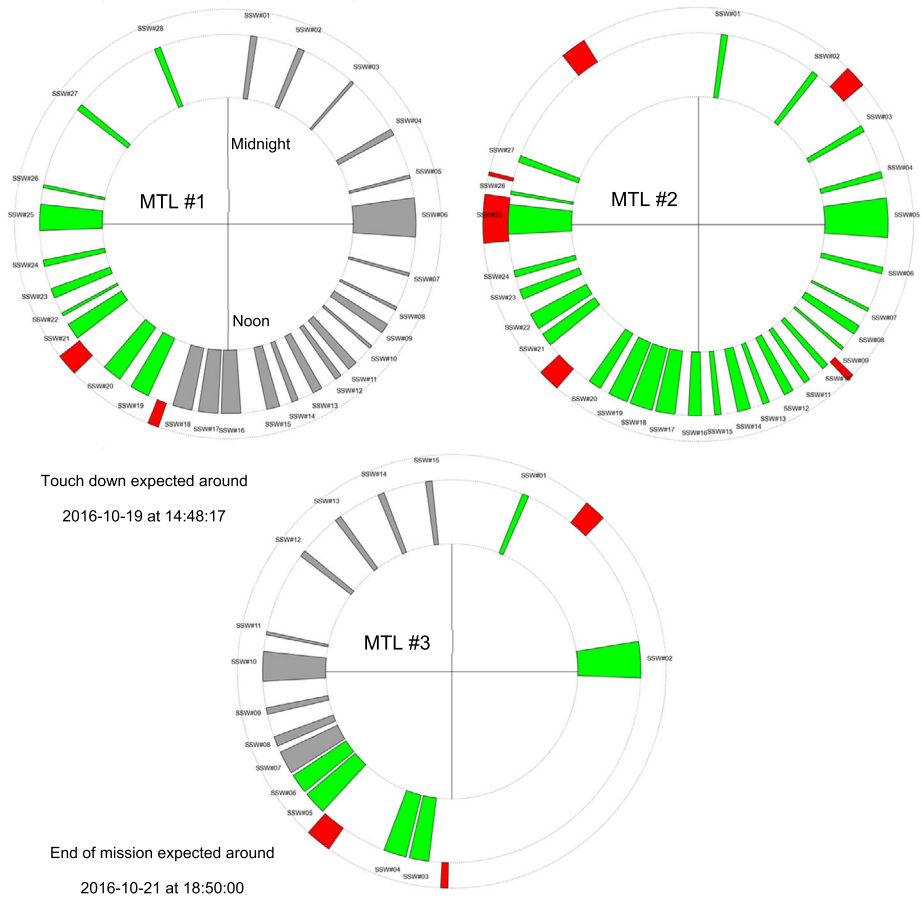


Fig. 23 Final surface timeline. Gray markers are the sensor acquisitions not executed, green are executed, while red markers are the communication windows with the descent module

green markers in Fig. 23). During each SSW all the sensors are acquired simultaneously with different configurations depending on the local time. The overall data volume uploaded to the descent module is about 118 Mbit over 2 sols. The internal battery depletion was expected around 2016-10-21 at 18:50:00. Nevertheless, the MTLs contains additional SSWs (gray markers) that could be executed in an extended mission. The energy stored in the battery depends on the thermal conditions experienced by the instrument during the cruise and at the surface, hence a warmer environment could result in more energy available for the experiment.

6 Conclusions

The Schiaparelli module of the ExoMars 2016 mission accommodated the DREAMS (Dust Characterization, Risk Assessment and Environmental Analyzer on the Martian Surface) experiment. DREAMS is a small meteorological station with the capability to measure electrical fields at the Martian surface. It includes six sensors: MarsTEM (thermometer), MetWind

Table 4 Sensor acquisition sequences foreseen during the nominal DREAMS mission

MIL	SSW	UTC	Local time	Time [s]	Data [Mbit]
1	19	20161019T15:12:20.000	13:40:00.808	1528	6.559
	20	20161019T15:53:27.000	14:20:00.773	1530	6.616
	21	20161019T17:10:32.000	15:35:00.100	1117	3.097
	22	20161019T17:41:23.000	16:05:00.803	406	1.057
	23	20161019T18:07:04.000	16:29:59.930	762	2.178
	24	20161019T18:48:11.000	17:09:59.895	406	1.057
	25	20161019T19:31:22.000	17:52:00.489	2182	5.527
	26	20161019T20:25:51.000	18:45:00.660	393	0.211
2	27	20161019T22:13:47.000	20:30:00.686	393	0.163
	28	20161020T00:17:08.000	22:30:00.574	393	0.163
	1	20161020T02:20:30.000	00:30:01.432	393	0.171
	2	20161020T04:23:51.000	02:30:01.316	393	0.163
	3	20161020T05:56:21.000	04:00:00.497	395	0.325
	4	20161020T06:58:02.000	05:00:00.923	393	0.211
	5	20161020T07:28:52.000	05:30:00.650	2905	7.470
	6	20161020T08:56:15.000	06:55:01.171	393	0.211
	7	20161020T09:47:38.000	07:45:00.390	393	0.171
	8	20161020T10:13:20.000	08:10:00.485	735	0.382
	9	20161020T10:44:11.000	08:40:01.184	393	0.171
	10	20161020T11:15:01.000	09:10:00.909	393	0.171
	11	20161020T11:45:51.000	09:40:00.635	393	0.171
	12	20161020T12:06:25.000	10:00:01.100	767	2.455
	13	20161020T12:42:23.000	10:35:00.455	408	1.195
	14	20161020T13:08:05.000	11:00:00.550	767	2.455
	15	20161020T13:44:04.000	11:35:00.877	408	1.195
	16	20161020T14:09:46.000	12:00:00.972	767	2.455
	17	20161020T14:40:36.000	12:30:00.696	1552	7.559
	18	20161020T15:11:26.000	13:00:00.421	1552	7.559
	19	20161020T15:42:17.000	13:30:01.118	1552	7.559
	20	20161020T16:18:15.000	14:05:00.471	1127	3.633
	21	20161020T17:40:29.000	15:25:00.383	1127	3.633
	22	20161020T18:06:11.000	15:50:00.477	1127	3.633
	23	20161020T18:47:18.000	16:30:00.432	769	2.544
	24	20161020T19:18:08.000	17:00:00.155	408	1.244
	25	20161020T20:11:36.000	17:52:00.972	2096	0.813
26	20161020T20:57:51.000	18:37:00.556	408	1.195	
27	20161020T21:42:03.000	19:20:00.483	408	1.195	
3	1	20161021T04:02:23.000	01:30:00.290	407	1.130
	2	20161021T08:03:57.000	05:25:00.367	2892	6.958
	3	20161021T15:20:49.000	12:29:59.946	1484	4.527
	4	20161021T15:51:40.000	13:00:00.636	1484	4.527
	5	20161021T17:49:52.000	14:54:59.875	1546	7.315
	6	20161021T18:20:43.000	15:25:00.565	1546	7.315
Tot.				40891	118

(anemometer), DREAMS-P (pressure sensor), DREAMS-H (humidity sensor), SIS (Solar Irradiance Sensor) and MicroARES (electric field sensor), a Common Electronic Unit and a Battery. It can operate autonomously according to a Mission Time Line and provide environmental measurements at the surface of Mars, including the first ever investigation of atmospheric electric phenomena. It can be accommodated on any short or long duration platform on the Martian surface.

DREAMS is an autonomous instrument suite with an internal power supply unit. It has been designed to survive and operate in extremely dusty conditions. Its overall mass is 4362 g including the battery (1691 g) and the harness. Its power consumption at the nominal battery voltage of 28 V is 5.60 W when in Cruise and Surface states, 7.84 W during acquisition, 6.72 W in Upload state and 0.28 W in idle state. DREAMS has been fully calibrated and tested in the field. It performed nominally during the cruise to Mars and was healthy during the descent to Mars. A Spare Model of the instrument, identical to the one flown on-board Schiaparelli is available for a future mission.

Acknowledgements This work was supported by the Italian Space Agency through the agreement I/018/12/0: "DREAMS EDM Payload ExoMars 2016." The development of the DREAMS instrument was funded and coordinated by ASI.

DREAMS is the result of a cooperation of six European Countries (Italy, France, Spain, Netherlands, Finland, United Kingdom) led by Italy. DREAMS is built by UPD-CISAS with contribution from LAT-MOS/FMI/INTA/Oxford University/INAF-OAC, operated by INAF-OAC/UPD-CISAS and provided by ASI.

Appendix

List of Acronyms

AC	Alternating Current
ADC	Analog to Digital Converter
AM0	Air Mass 0
CEU	Central Electronic Unit
CFD	Computational Fluid Dynamics
COTS	Commercial-Of-The-Shelf
CPU	Central Processing Unit
DC	Direct Current
DREAMS	Dust characterization, Risk assessment and Environment Analyzer on the Martian Surface
DSP	Digital Signal Processor
EDM	Entry descent and landing Demonstrator Module
E-field	Electric field
ESA	European Space Agency
FM	Flight Model
FMI	Finnish Meteorological Institute
FoV	Field of View
FPGA	Field-Programmable Gate Array
FS	Flight Spare
HK	Housekeeping
INTA	Instituto Nacional de Técnica Aeroespacial
ISO	International Standards Organization
LTST	Local True Solar Time
MCU	Microcontroller Unit

MEMS	Micro Electro-Mechanical System
MSL	Mars Science Laboratory
MTL	Mission TimeLine
NASA	National Aeronautics and Space Administration
NIR	Near Infrared
OBDH	On-Board Data Handling
OD	Optical Depth
OH	Optical Head
P1/P2	DREAMS Pressure Sensor 1/2
PCB	Printed Circuit Board
PDS4	Planetary Data System version 4
PE	Processing Electronics
PTFE	Polytetrafluoroethylene
RDS	Radiation and Dust Sensor
REF	Ground reference model
REMS	Rover Environmental Monitoring Station
RH	Relative Humidity
RTD	Resistance Temperature Detector
SIS	Solar Irradiance Sensor
SNR	Signal to Noise Ratio
SPASOLAB	Space Solar Cell Test Laboratory
SSW	Sensor SWitch sequence
SZA	Solar Zenith Angle
TID	Total ionizing Dose
TGO	Trace Gas Orbiter
TVT	Thermal Vacuum Test
UHF	Ultra High Frequency
UTC	Universal Time Coordinated
UV	UltraViolet

References

- M. Álvarez, C. Hernando, J.J. Jiménez, F.J. Álvarez, I. Martín, D. Escribano, TID results of optical materials and photodiodes for SIS instruments (DREAMS project), in *Proc. of IEEE Nuclear and Space Radiation Effects Conference*, Paris, France (2014)
- M. Álvarez, J.J. Jiménez, D. Escribano, P. Manzano, I. Arruego, V. Apéstigue, M. González-Guerrero, Low dose rate TID testing of ADXL327 accelerometer for a Mars mission, in *Proc. of IEEE Nuclear and Space Radiation Effects Conference*, Boston, Massachusetts (2015)
- V. Apéstigue, I. Arruego, J. Martínez, J.J. Jiménez, J. Rivas, M. González, J. Álvarez, J. Azcue, A. Martín-Ortega, J.R. de Mingo, M.T. Álvarez, L. Bastide, A. Carretero, A. Santiago, I. Martín, B. Martín, M.A. Alcacera, J. Manzano, T. Belenger, R. López, D. Escribano, P. Manzano, J. Boland, E. Cordoba, A. Sánchez-Lavega, S. Pérez, A. Sainz López, M. Lemmon, M. Smith, C.E. Newman, J. Gómez Elvira, N. Bridges, P. Conrad, M. de la Torre Juárez, R. Urqui, J.A. Rodríguez Manfredi, Radiation and Dust Sensor for MARS2020: technical design and development status overview, in *Proc. of European Planetary Science Congress*, vol. 10 (2015)
- K.L. Aplin, Atmospheric electrification in the Solar System. *Surv. Geophys.* **27**(1), 63–108 (2006). <https://doi.org/10.1007/s10712-005-0642-9>
- I. Arruego, V. Apéstigue, J. Jiménez-Martín, J. Martínez-Oter, F.J. Álvarez-Ríos, M. González-Guerrero, J. Rivas, J. Azcue, I. Martín, D. Toledo, L. Gómez, M. Jiménez-Michavila, M. Yela, DREAMS-SIS: the Solar Irradiance Sensor on-board the ExoMars 2016 Lander. *Adv. Space Res.* **60**, 103–120 (2017)
- S.K. Atreya, A.-S. Wong, N.O. Renno, W.M. Farrell, G.T. Delory, D.D. Sentman, S.A. Cummer, J.R. Marshall, S.C.R. Rafkin, D.C. Catling, Oxidant enhancement in Martian dust devils and storms: implications for life and habitability. *Astrobiology* **6**(3), 439–450 (2006)

- J. Berthelier, R. Grard, H. Laakso, M. Parrot, ARES, atmospheric relaxation and electric field sensor, the electric field experiment on NETLANDER. *Planet. Space Sci.* **48**, 1193–1200 (2000). [https://doi.org/10.1016/S0032-0633\(00\)00103-3](https://doi.org/10.1016/S0032-0633(00)00103-3)
- T. Bertrand, A. Spiga, S. Rafkin, A. Colaitis, F. Forget, E. Millour, An intercomparison of large-eddy simulations of the Martian daytime convective boundary layer. *Geosci. Model Dev. Discuss.* (2016). <https://doi.org/10.5194/gmd-2016-241>
- N. Bridges, P. Geissler, S. Silvestro, M. Banks, Bedform migration on Mars: current results and future plans. *Aeolian Res.* **9**, 133–151 (2013). <https://doi.org/10.1016/j.aeolia.2013.02.004>
- S. Chiodini, G. Colombatti, M. Pertile, S. Debei, Numerical study of lander effects on DREAMS scientific package measurements, in *IEEE Metrology for Aerospace (MetroAeroSpace)* (2014), pp. 433–438
- S. Chiodini, G. Colombatti, E. Friso, M. Pertile, S. Debei, Multiphysics modelling of MarsTEM shield, in *2015 IEEE Metrology for Aerospace (MetroAeroSpace)* (2015), pp. 271–276
- M. Chojnacki, A. Urso, L.K. Fenton, T.I. Michaels, Aeolian dune sediment flux heterogeneity in Meridiani Planum, Mars. *Aeolian Res.* **26** (2017)
- G. Colombatti, S. Chiodini, E. Friso, A. Aboudan, C. Bettanini, S. Debei, F. Esposito, MarsTEM: the temperature sensor of the DREAMS package onboard Exomars2016, in *2014 IEEE Metrology for Aerospace (MetroAeroSpace)* (2014), pp. 249–254
- G. Colombatti, S. Chiodini, E. Friso, A. Aboudan, C. Bettanini, M. Poli, S. Debei, F. Esposito, C. Molfese, P. Schipani, R. Mugnuolo, S. Pirrotta, E. Marchetti, Marstem field test in Mars analog environment, in *2015 IEEE Metrology for Aerospace (MetroAeroSpace)* (2015)
- G. Déprez, Micro-ARES on ExoMars 2016. PhD thesis (2016, to be published)
- F. Esposito, R. Molinaro, C.I. Popa, A. Molfese, F. Cozzolino, L. Marty, K. Taj-Eddine, G. Di Achille, G. Franzese, S. Silvestro, G.G. Ori, The role of the atmospheric electric field in the dust-lifting process. *Geophys. Res. Lett.* **43** (2016). <https://doi.org/10.1002/2016GL068463>
- W.M. Farrell, J.L. McLain, M.R. Collier, J.W. Keller, T.J. Jackson, G.T. Delory, Is the electron avalanche process in a martian dust devil self-quenching? *Icarus* **254**, 333–337 (2015). <https://doi.org/10.1016/j.icarus.2015.04.003>
- V. Formisano, S. Atreya, T. Encrenaz, N. Ignatiev, M. Giuranna, Detection of methane in the atmosphere of Mars. *Science* **306**(5702), 1758–1761 (2004)
- A.-M. Harri, M. Genzer, O. Kempainen, J. Kahanpää, J. Gomez-Elvira, J.A. Rodriguez-Manfredi, R. Haberle, J. Polkko, W. Schmidt, H. Savijärvi, J. Kauhanen, E. Atkaslin, M. Richardson, T. Siili, M. Paton, M. de La TorreJuarez, C. Newman, S. Rafkin, M.T. Lemmon, M. Mischna, S. Merikallio, H. Haukka, J. Martin-Torres, M.-P. Zorzano, V. Peinado, R. Urqui, A. Lepinette, A. Scodary, T. Mäkinen, L. Vazquez, N. Rennó (the REMS/MSL Science Team), Pressure observations by the curiosity rover—initial results. *J. Geophys. Res.* **119**, 82–92 (2014a)
- A.-M. Harri, M. Genzer, O. Kempainen, J. Gomez-Elvira, R. Haberle, J. Polkko, H. Savijärvi, N. Rennó, J.A. Rodriguez-Manfredi, W. Schmidt, M. Richardson, T. Siili, M. Paton, M. de la Torre-Juarez, T. Mäkinen, C. Newman, S. Rafkin, M. Mischna, S. Merikallio, H. Haukka, J. Martin-Torres, M. Komu, M.-P. Zorzano, V. Peinado, L. Vazquez, R. Urqui, Mars Science Laboratory relative humidity observations—initial results. *J. Geophys. Res.* **119**, 2132–2147 (2014b)
- R.G. Harrison, E. Barth, F. Esposito, J. Merrison, F. Montmessin, K.L. Aplin, C. Borlina, J.J. Berthelier, G. Déprez, W. Farrell, I.M.P. Houghton, N.O. Renno, K.A. Nicoll, S.N. Tripathi, M. Zimmerman, Applications of electrified dust and dust devil electrodynamics to Martian atmospheric electricity. *Space Sci. Rev.* (2016). <https://doi.org/10.1007/s11214-016-0241-8>
- C. Holstein-Rathlou, J. Merrison, J.J. Iversen, A.B. Jakobsen, R. Nicolajsen, P. Nørnberg, K. Rasmussen, A. Merlone, G. Lopardo, T. Hudson, D. Banfield, G. Portyankina, An environmental wind tunnel facility for testing meteorological sensor systems. *J. Atmos. Ocean. Technol.* **31**(2), 447–457 (2014)
- J.J. Jimenez, J.M. Oter, V. Apestigue, C. Hernando, S. Ibarria, W. Hajdas, J. Sanchez-Paramo, M.T. Alvarez, I. Arruego, H. Guerrero, Proton monitor Las Dos Torres: first intercomparison of in-orbit results. *IEEE Trans. Nucl. Sci.* **59**(4) (2012)
- J.J. Jiménez, F.J. Álvarez, M. Gonzalez-Guerrero, V. Apéstigue, I. Martín, J.M. Fernández, A.A. Fernán, I. Arruego, Calibration OGSE for a multichannel radiometer for Mars atmosphere studies, in *Proc. of International Conference on Space Optics, ICSO*, Biarritz, France (2016)
- M.J. Mumma, G.L. Villanueva, R.E. Novak, T. Hewagama, B.P. Bonev, M.A. DiSanti, A.M. Mandell, M.D. Smith, Strong release of methane on Mars in northern summer 2003. *Science* **323**(5917), 1041 (2009)
- J. Murphy, K. Steakley, M. Balme, G. Deprez, F. Esposito, H. Kahanpää, M. Lemmon, R. Lorenz, N. Murdoch, L. Neakrase, M. Patel, P. Whelley, Field measurements of terrestrial and Martian dust devils. *Space Sci. Rev.* (2016). <https://doi.org/10.1007/s11214-016-0283-y>
- T. Nikkanen, W. Schmidt, A.-M. Harri, M. Genzer, M. Hieta, H. Haukka, O. Kempainen, Space qualification of an automotive microcontroller for the DREAMS-P/H pressure and humidity instrument on board the ExoMars 2016 Schiaparelli lander, *EPCS2015-465* (2015)

- P. Schipani, L. Marty, M. Manna, F. Esposito, C. Molfese, A. Aboudan, V. Apestigue-Palacio, I. Arruego-Rodríguez, C. Bettanini, G. Colombatti, S. Debei, M. Genzer, A.-M. Harri, E. Marchetti, F. Montmessin, R. Mugnuolo, S. Pirrotta, C. Wilson, The ExoMars DREAMS scientific data archive. *Proc. SPIE* **9913**, 99134F (2016)
- A. Seiff, J.E. Tillman, J.R. Murphy, J.T. Schofield, D. Crisp, J.R. Barnes, C. LaBaw, C. Mahoney, J.D. Mihalov, G.R. Wilson, R. Haberle, The atmosphere structure and meteorology instrument on the Mars Pathfinder lander. *J. Geophys. Res.* **102**(E2), 4045–4056 (1997)
- S. Silvestro, D.A. Vaz, L.K. Fenton, P.E. Geissler, Active aeolian processes on Mars: a regional study in Arabia and Meridiani Terrae. *Geophys. Res. Lett.*, L20201 (2011). <https://doi.org/10.1029/2011GL048955>
- S. Silvestro, D.A. Vaz, G. Di Achille, I.C. Popa, F. Esposito, Evidence for different episodes of aeolian construction and a new type of wind streak in the 2016 ESA ExoMars landing ellipse in Meridiani Planum, Mars. *J. Geophys. Res., Planets* **120**(4), 760–774 (2015). <https://doi.org/10.1002/2014JE004756>
- M.D. Smith, M.-P. Zorzano, M. Lemmon, J. Martín-Torres, T. Mendaza de Cal, Aerosol optical depth as observed by the Mars Science Laboratory REMS UV photodiodes. *Icarus* **280**, 234–248 (2016)
- D. Toledo, I. Arruego, V. Apéstigue, J.J. Jiménez, L. Gómez, M. Yela, P. Rannou, J.-P. Pommereau, Measurement of dust optical depth using the solar irradiance sensor (SIS) onboard the ExoMars 2016 EDM. *Planet. Space Sci.* **138**, 33–43 (2017)
- M.C. Townner, M.R. Patel, T.J. Ringrose, J.C. Zarnecki, D. Pullan, M.R. Sims, S. Haapanala, A.M. Harri, J. Polkko, C.F. Wilson, A.P. Zent, R.C. Quinn, F.J. Grunthaner, M.H. Hecht, J.R.C. Garry, The Beagle 2 environmental sensors: science goals and instrument description. *Planet. Space Sci.* **52**, 1141–1156 (2004)
- J. Vago, O. Witasse, H. Svedhem, P. Baglioni, A. Haldemann, G. Gianfiglio, T. Blancquaert, D. McCoy, R. de Groot, ESA ExoMars program: the next step in exploring Mars. *Sol. Syst. Res.* **49**(7), 518–528 (2015)
- I. Vidali, MarsTEM, un termometro per la misura della temperatura atmosferica marziana: progettazione, prototipazione e studio degli effetti dovuti all'autoriscaldamento. Bachelor Thesis, Padova Univ. (2012)
- C.R. Webster, P.R. Mahaffy, S.K. Atreya, G.J. Flesch, M.A. Mischna, P.-Y. Meslin, K.A. Farley, P.G. Conrad, L.E. Christensen, A.A. Pavlov, J. Martín-Torres, M.-P. Zorzano, T.H. McConnochie, T. Owen, J.L. Eigenbrode, D.P. Glavin, A. Steele, C.A. Malespin, P.D. Archer, B. Sutter Jr., P. Coll, C. Freissinet, C.P. McKay, J.E. Moores, S.P. Schwenzer, J.C. Bridges, R. Navarro-Gonzalez, R. Gellert, M.T. Lemmon (the MSL Science Team), Mars methane detection and variability at Gale crater. *Science* **347**(6220), 415–417 (2015)
- C.F. Wilson, Measurement of wind on the surface of Mars. DPhil thesis (2003)
- C.F. Wilson, S.B. Calcutt, T.V. Jones, The Beagle 2 wind sensor, EGS–AGU–EUG Joint Assembly, abstract #691 (2003)
- C.F. Wilson, A.L. Camilletti, S.B. Calcutt, P.M. Ligrani, A wind tunnel for the calibration of Mars wind sensors. *Planet. Space Sci.* **56**(11), 1532–1541 (2008). <https://doi.org/10.1016/j.pss.2008.05.011>